AUTOMATED FAULT SCARP OFFSET ANALYSES APPLIED TO

THE NEPHI SEGMENT OF THE WASATCH FAULT, UTAH

UTILIZING LIDAR-DERIVED, HIGH-RESOLUTION

DIGITAL ELEVATION MODELS

by

Billie John Smathers

A thesis submitted to the faculty of
The University of Utah
in partial fulfillment of the requirements for the degree of

Master of Science

in

Geology

Department of Geology and Geophysics

The University of Utah

May 2015

The University of Utah Graduate School

STATEMENT OF THESIS APPROVAL

The thesis of   **Billie John Smathers**

has been approved by the following supervisory committee members:

| **Ronald Bruhn** | , Chair | **10/6/2014** |
| | | Date Approved |

| **Paul Jewell** | , Member | **10/30/2014** |
| | | Date Approved |

| **Christopher DuRoss** | , Member | **10/21/2014** |
| | | Date Approved |

and by   **John Bartley**   , Chair/Dean of

the Department/College/School of   **Geology and Geophysics**

and by David B. Kieda, Dean of The Graduate School.

ABSTRACT

This thesis describes the development of software used to extract and analyze topographic profiles of normal fault scarps from high-resolution LiDAR (Light Detection and Ranging) digital elevation models. The software, 'Scarp Offset Analysis' (SOA), consists of several scripts written in the Python computer language that partly automate the extraction of fault scarp parameters including surface offset, scarp asymmetry, location and magnitude of maximum scarp slope, far-field slopes, and the location of the scarp's base and crest. These parameters were calculated from 36,757 topographic profiles extracted every 1 m along ~37 km of the Nephi segment of the Wasatch fault. The profiles were extracted from bare earth digital elevation models (DEMs) derived from high-resolution (0.5-m horizontal posting) LiDAR elevation data.

The scarp profiles provide information on individual scarps and as a whole, provide a dense network for analyzing spatial trends in fault offset along strike at scales from meters to tens of kilometers. The surface offset measurements are also utilized to produce a prototype 3D probability function (3D-PDF), which is an along strike graphical representation of trends in surface offset expressed as a probability density plot. The 3D-PDF function is used to evaluate several hypothetical models of fault displacement along strike, as a prototype application to illustrate the potential use of SOA software in paleoseismic studies. Application of the 3D-PDF to the Nephi segment suggests unique rupture profiles for the northern and southern fault strands; however, interpretation of the

3D-PDF is inhibited by the lack of detailed information concerning the age of alluvial surfaces offset by faulting. Ultimately, the SOA software is an important tool for studying fault scarp morphology, which can be applied to other LiDAR datasets and also adapted for use in the study of fluvial terraces, lacustrine and marine shoreline scarps, and similar geomorphic features.

TABLE OF CONTENTS

ACKNOWLEDGMENTS

First, I would like to thank my wife, Paige, for all her love, support, work, patience, and encouragement throughout this process. I would also like to thank her for giving me my beautiful daughter, Aspen, during my thesis work. She may have slowed my progress but has made every day more joyful. I would also like to thank my advisor, Ron Bruhn, who instead of coasting into retirement took a lost graduate student under his wing. Thank you for making my time at the University of Utah a success. Thanks to Chris DuRoss for his guidance and discussions that helped inspire and focus the latter end of my research. Thanks also to Paul Jewell for his work on my committee and for his encouragement to present my research at AEG.

Lastly, I would like to thank everyone who has helped me along the way. My family provided much needed support, especially my mother and father. Thanks to Kevin Gardner for taking a crash course in Quaternary geology as my field assistant. Thanks to the many people who volunteered their time to babysit Aspen so that I could finish my thesis in a timely manner including Jo Smathers, Paula Henry, Lindsay Burton, and Kelli Green.

CHAPTER 1

INTRODUCTION

Topographic data are a key tool in geologic and geomorphologic investigations such as paleoseismic studies of prehistoric surface faulting on Holocene-active faults. LiDAR (Light Designation and Ranging) is a remote sensing technique utilized to produce topographic data, including bare earth digital elevation models (DEMs). Increasing improvements in LiDAR resolution and processing techniques have made high-resolution (0.1-1 m horizontal posting) bare earth DEMs available (Arrowsmith et al., 2008). These high-resolution data have made detailed topographic analyses, such as hydrologic (e.g., stream profiling and drainage-basin analysis) and fault-geomorphology (e.g., scarp profiling) analyses over large areas possible.

I developed SOA, a software application abbreviated for 'scarp offset analysis,' to automate the extraction of scarp morphological parameters including: surface offset, location and magnitude of maximum slope, far-field slope, and location of the scarp's base and crest. SOA was used to produce thousands of surface offset measurements from scarp topographic profiles, which characterize along strike fault offset patterns and model fault behavior over time. I utilized LiDAR-derived, high-resolution DEMs (herein: LiDAR DEMs) of part of the Nephi segment of the Wasatch fault in the development of this software. The Nephi LiDAR survey and general benefits of LiDAR data analysis are described below, before discussing the SOA software that was developed as the primary

goal of this thesis work.

Nephi Segment Dataset

In 2008, LiDAR data were obtained for a ~85 km^2 area along the Nephi segment of the Wasatch fault (Figure 1) yielding high-resolution (0.5 m horizontal gridded) bare earth DEMs (Figure 2). Using these data, I conducted a detailed morphologic analysis of fault scarps along ~30 km of the Nephi segment. Data were acquired by the National Center for Airborne Laser Mapping (http://www.ncalm.org) as part of the GeoEarthscope program of the National Science Foundation. These data are available for download at opentopography.org.

Nephi Segment of the Wasatch Fault

The Nephi segment is a 42-km long segment of the Wasatch normal fault, which bounds the eastern Basin and Range Province in central Utah. The Nephi segment has two distinct strands, referred to in this report as the northern and southern strands. The 17 km northern strand and the 25 km southern strand are separated by a ~5 km right step. Both strands have evidence for multiple late Quaternary surface-faulting earthquakes (Machette, 1992; DuRoss and Bruhn 2005). The Nephi segment is bounded to the north by the Payson salient (segment boundary with the Provo segment) and to the south by the Levan segment. At the Payson salient, the Provo segment overlaps with the Nephi segment, forming a ~9 km-wide en echelon right step (Machette, 1992). The Nephi and Levan segments are separated by a 15 km gap in Holocene and latest Pleistocene surface faulting (Machette, 1992; Hylland and Machette, 2008).

Fault scarps along the Nephi segment offset late Pleistocene to Holocene surfaces including alluvial fans, colluvium, landslides, debris flows, and Lake Bonneville deposits

(Harty et al, 1997). These fault scarps are generally well preserved and have undergone little to no anthropogenic alteration. However, much of the fault is located at the base of the mountain where it forms the contact between bedrock and the surficial deposits.

The Nephi segment has undergone a wide range of studies including surface geology mapping (Harty et al., 1997), fault scarp profiling (DuRoss and Bruhn, 2005), fault scarp diffusion modeling (Mattson and Bruhn, 2001; DuRoss and Bruhn, 2005), and paleoseismic fault scarp trenching investigations (Hanson et al., 1981; Jackson, 1991; Machette et al., 2007; DuRoss et al., 2008). Paleoseismic trench investigations found evidence of three recent (late Holocene) surface faulting events. The paleoseismic investigations along with fault scarp diffusion modeling constrain a slip rate from 0.5-3.0 mm/yr during the period encompassing the three surface-rupturing events, while longer-term (late Pleistocene) slip rates are as low as 0.2 mm/yr. The Nephi segment's recent surface faulting history, lack of anthropogenic alteration, and availability of high-resolution LiDAR data make it a perfect choice for application and testing of SOA during development of the software.
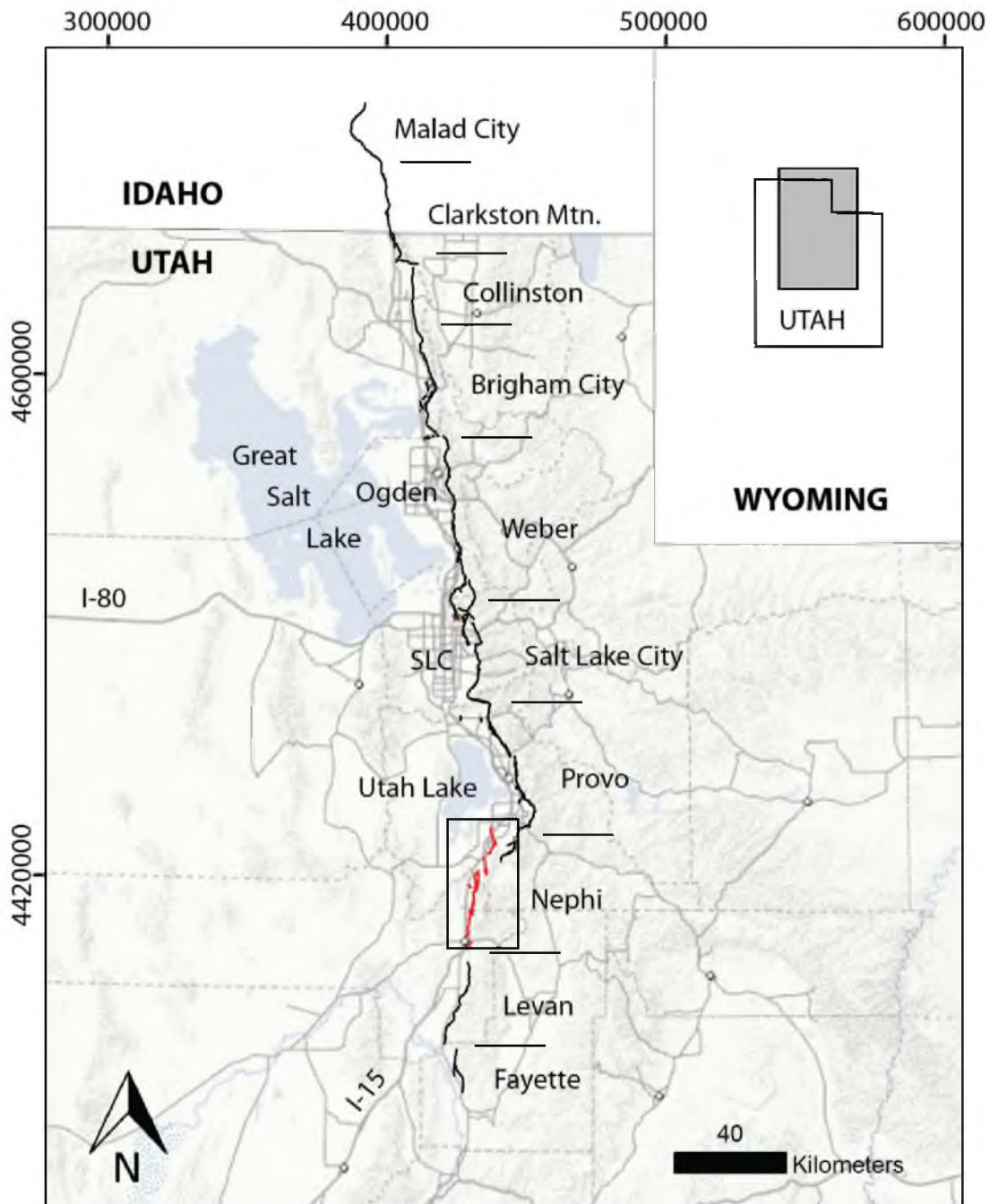
Figure 1: Segments of the Wasatch fault (heavy lines) from the Quaternary Fault and Fold Database for the United States (U.S. Geological Survey et al., 2006). Horizontal lines to the right of the fault trace indicate segment boundaries. The Nephi segment of the Wasatch fault is highlighted in red. Box indicates location of Figure 2.
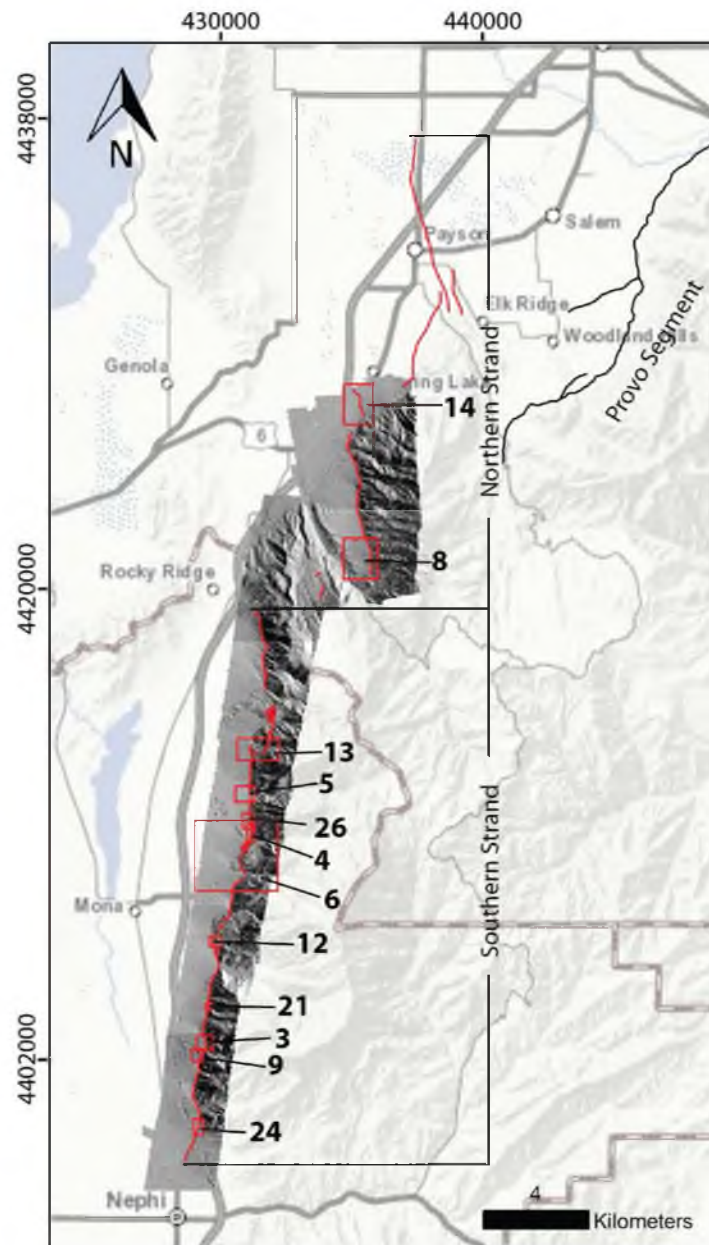
Figure 2: LiDAR survey of the Nephi segment. Hillshade map indicates the extent of LiDAR-derived DEM coverage. Red line indicates fault trace of the Nephi segment and black line indicates fault trace of the Provo segment. The author mapped the fault trace within the DEM coverage while the fault trace outside the DEM coverage was obtained from the Quaternary Fault and Fold Database for the United States (U.S. Geological Survey et al., 2006). Northern and southern strands of the Nephi segment indicated by black, bracketing lines. Red boxes indicate figure locations with figure number indicated to the right of the box.

CHAPTER 2

LIDAR BENEFITS AND DETAILS

LiDAR Benefits

<u>Bare Earth Model</u>

One of the greatest benefits of acquiring high-resolution LiDAR data is the ability

to create bare earth DEM models (Haugerud et al., 2003). During data acquisition, a laser

mounted on an aircraft is pulsed at the ground surface. When surveying over vegetation, a

single laser pulse will have multiple reflections due to sampling various parts of the

vegetation as well as the ground surface. These reflections are processed into

geodetically-referenced elevation data points (elevation point cloud). The point cloud is

processed (typically by the vendor) to remove reflections from vegetation, buildings, and

other infrastructure yielding ground-surface elevation points that are processed into a

gridded bare earth DEM, a 3D digital model of the ground surface.

Bare earth DEMs allow for the identification of features that were previously

obscured due to thick vegetation cover (Harding and Berghoff, 2000). For example,

previously undiscovered surface rupturing faults, landslides, uplifted beaches, and glacial

features have been revealed in high-resolution bare earth DEMs of the Puget lowland

(Haugerud et al., 2003).

The benefits of a bare earth elevation model are not limited to mapping the fault

trace. As a part of this thesis, a detailed fault scarp offset analysis was performed to

determine vertical tectonic displacements along the length of the Nephi fault segment.

The bare earth model allowed fault scarp profiles to be analyzed every 1 m along the

entire length of the segment. Without the bare earth model the sampling of fault scarp

profiles would have been limited to areas with little or no vegetation. The removal of

vegetation by filtering of reflections allows surface features to be analyzed without

significant uncertainty caused by errors introduced by masking of the earth's surface

beneath vegetation (Haugerud et al., 2003).

Efficiency

High-resolution bare earth LiDAR DEMs allow the detection of very subtle

topographic features (Webster et al., 2006; Lin et al., 2013; Robinson et al., 2012) and

also make detailed topographic analysis over large regions possible (Glenn et al, 2006).

As part of this thesis, fault scarp profiles were surveyed in the field using a laser range

finder. It took one day to survey five scarp profiles at different locations along the Nephi

segment. To extract the same five profiles with similar resolution and accuracy from the

LiDAR DEM took ten minutes. With custom-made software applications, the advantage

of utilizing LiDAR DEMs to map and analyze scarps is much more efficient than ground

surveying, although care must be taken to check the validity of the interpretations in the

field. Thousands of detailed measurements spread over large regions can be obtained

quickly at a modest cost of several hundred dollars per square kilometer for acquisition

and processing plus time spent on analysis and field checks. This results in the ability to

map and plot profiles in detail over tens of kilometers along a fault. LiDAR-derived

DEMs also lend themselves to 3D as well as 2D analysis. For example, LiDAR-derived

DEMs make analysis of a single fault scarp topographic profile possible as well as

analysis of along strike trends in fault scarp topographic profiles.

Benefits in Visualization

LiDAR-derived imagery can be utilized for geomorphic mapping in a manner similar to aerial photography. Most aerial photography is flown at midday to avoid shadows, which is not conducive to highlighting fault scarps that are best revealed when the sun angle is low and casts shadows on fault scarps facing away from the illumination, or alternatively, creates bright bands on scarps facing the sun. If low sunlight angle photos are available, they are limited to roughly an east or west sun azimuth; however, LiDAR-derived hillshade images can be produced at any sun angle and azimuth (Pavlis and Bruhn, 2011).

Many derivative products can be produced from the high-resolution LiDAR-derived DEMs (Klingebiel et al., 1988; U.S. Geological Survey, 1993). Products particularly useful for analyzing fault scarps and fluvial terrace risers include slope, slopeshade, aspect, and curvature maps. Slope maps highlight abrupt changes in slope (displaying the magnitude of the maximum change in elevation for each DEM cell), making them useful for identifying fault scarps, as well as their bases and crests (Sanders and Slemmons, 1996; Hooper et al., 2003; Ganas et al., 2005) (Figure 3A). Slope-shade maps are also useful for identifying antithetic scarps due to their ability to highlight slopes irrespective of their aspect or angle with respect to either natural or artificial sources of illumination (Crosby, 2012) (Figure 4). Because slope-shade maps highlight surface texture, they are also useful for determining relative ages of alluvial fans (Figure 5). An aspect map displays the compass direction that a topographic slope faces, and thus, is useful for delineating alluvial fan boundaries (Frankel et al., 2007). For example,

two alluvial fans originating from different source points may merge or overlap downstream. The merged fans typically have distinctly different aspects that are highlighted in an aspect map (Figure 6). A curvature map displays the second derivative of elevation (Figure 3B).

LiDAR Data Quality – Heterogeneity and Processing Artifacts

Causes of Data Heterogeneity

Data heterogeneity, or the spatial variability in point density, affects how well the ground surface is constrained throughout the dataset. Data acquisition flight plans are typically designed to perform long, straight flight paths to collect overlapping swaths of data over the area of interest. However, the actual flight lines are not perfectly linear due to factors such as aircraft instability, varying wind conditions, and navigation errors. Therefore, overlap coverage of swaths varies. The plane's velocity is also affected by similar factors. These incongruities in flight path overlap and the plane's velocity cause spatial variation in point density, examples of which can be seen in the Nephi dataset (Figure 7). While changes in aircraft velocity can cause small areas with abnormal point density, inadequate overlap of flight swaths can significantly reduce the point density coverage over a large percentage of the survey area.

Vegetation is another large source of data heterogeneity. When a laser pulse encounters bare ground it produces one reflection. Conversely, when a laser pulse encounters vegetation it produces multiple reflections. If a laser pulse is directed at a bush, part of the laser pulse will interact with the top leaves of the bush, part with branches and leaves further within the bush, and part of the laser pulse will reach the ground (Harding et al., 1994, 2001). These different interactions cause reflections to

return at slightly different times causing areas of vegetation to have high point density in the unfiltered data. However, when the data are properly filtered, all of the reflections from vegetation are removed causing areas of vegetation to have low point density in the filtered data (Figure 7). A noticeable decrease in point density in the northern section of the Nephi survey is attributed to more extensive and dense vegetation than in the southern section.

Artifacts

Artifacts are apparent surface features created during data processing and DEM modeling that are not true representations of the actual ground surface. If unrecognized, artifacts produce errors when extracting topographic profiles and other spatial variables from the DEM. Artifacts include holes in point density caused by aggressive filtering to remove vegetation (Figure 8), topographic 'mounds' where vegetation was not adequately filtered out of the signals (Figure 9), and spatial changes in point density related to variations in surface slope and flight path (Zhang and Whitman, 2005). When assessing the quality of LiDAR-derived DEMs, it is important to look for such processing artifacts to determine how well the ground surface is constrained at any given location. It is also important to take scale into consideration with these types of artifacts. For example, it is impossible to remove 100 percent of the vegetation reflections. While bumps may always be present, for some types of analysis they can become negligible at certain scales.

Kriging and triangulated irregular network (TIN) are two common methods of producing a DEM from LiDAR point cloud data. Visually determining areas of low point density on TIN models is much more straightforward than using kriging models due to

the easily recognizable, angular features of TIN artifacts. Kriging methods estimate the ground surface in areas of low point density by interpolating between data points, creating a smoothed ground surface. TIN methods create triangular facets between data points to model the ground surface. The TIN method creates smooth surfaces when data density is high, but when data density is low the triangular facets become quite large creating a sharp, angular ground surface model.

Figure 3: Comparison of A) hillshade (illumination azimuth is and 075 degrees and illumination angle is 45 degrees) and B) slope maps derived from bare earth DEMs. Although both maps highlight the steep fault scarp slope running vertically through the center of the map, in the slope map, the base and crest of the scarp are delineated by the abrupt transition from the steep scarp slope (red) to the gentler slopes (yellow and green). Slope angles vary from two degrees for green through a maximum of 50 degrees for red.
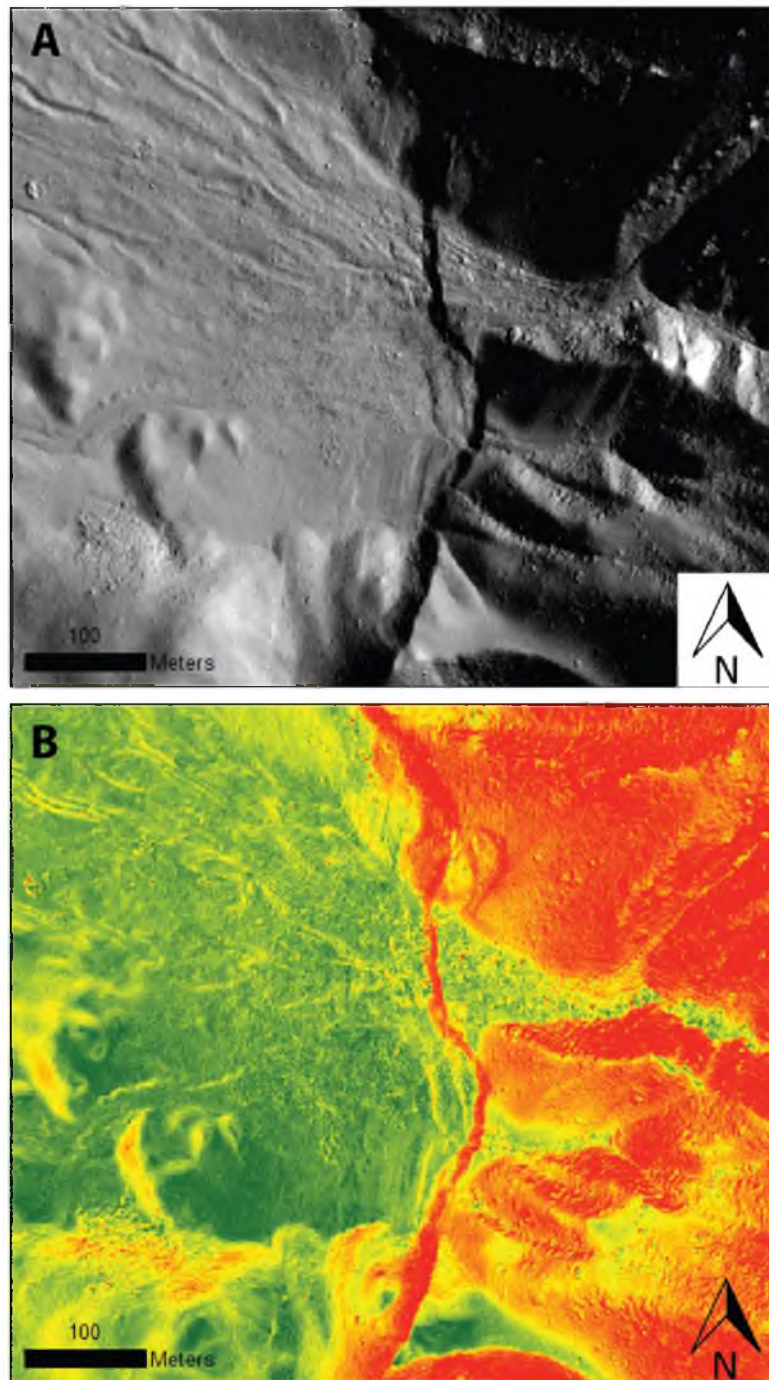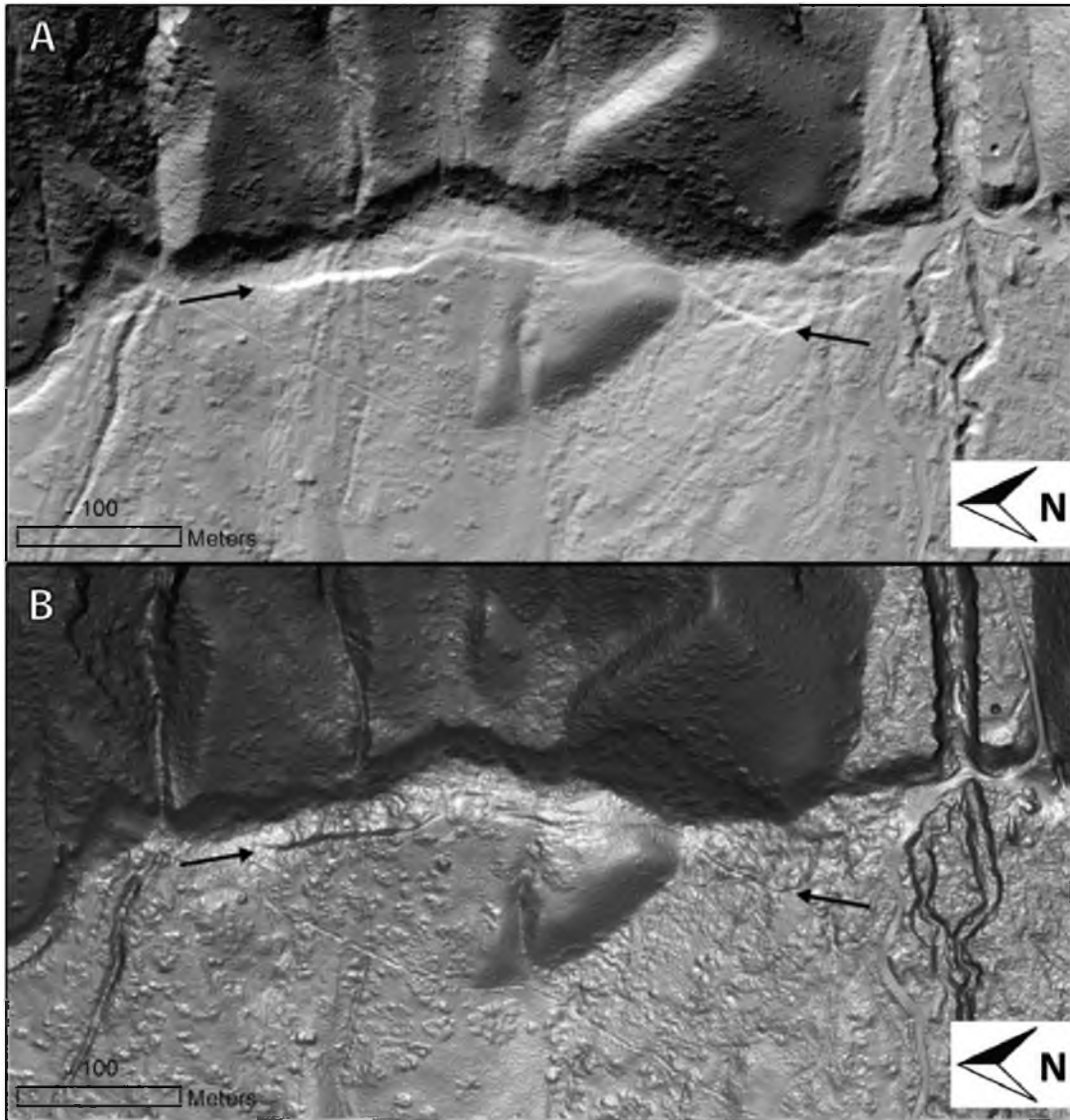
Figure 4: Comparison of A) hillshade (illumination azimuth is and 075 degrees and illumination angle is 45 degrees) and B) slopeshade maps. In the slopeshade map, steep surfaces (shadows) are shown regardless of their aspect, while the hillshade only shades slopes in one direction.
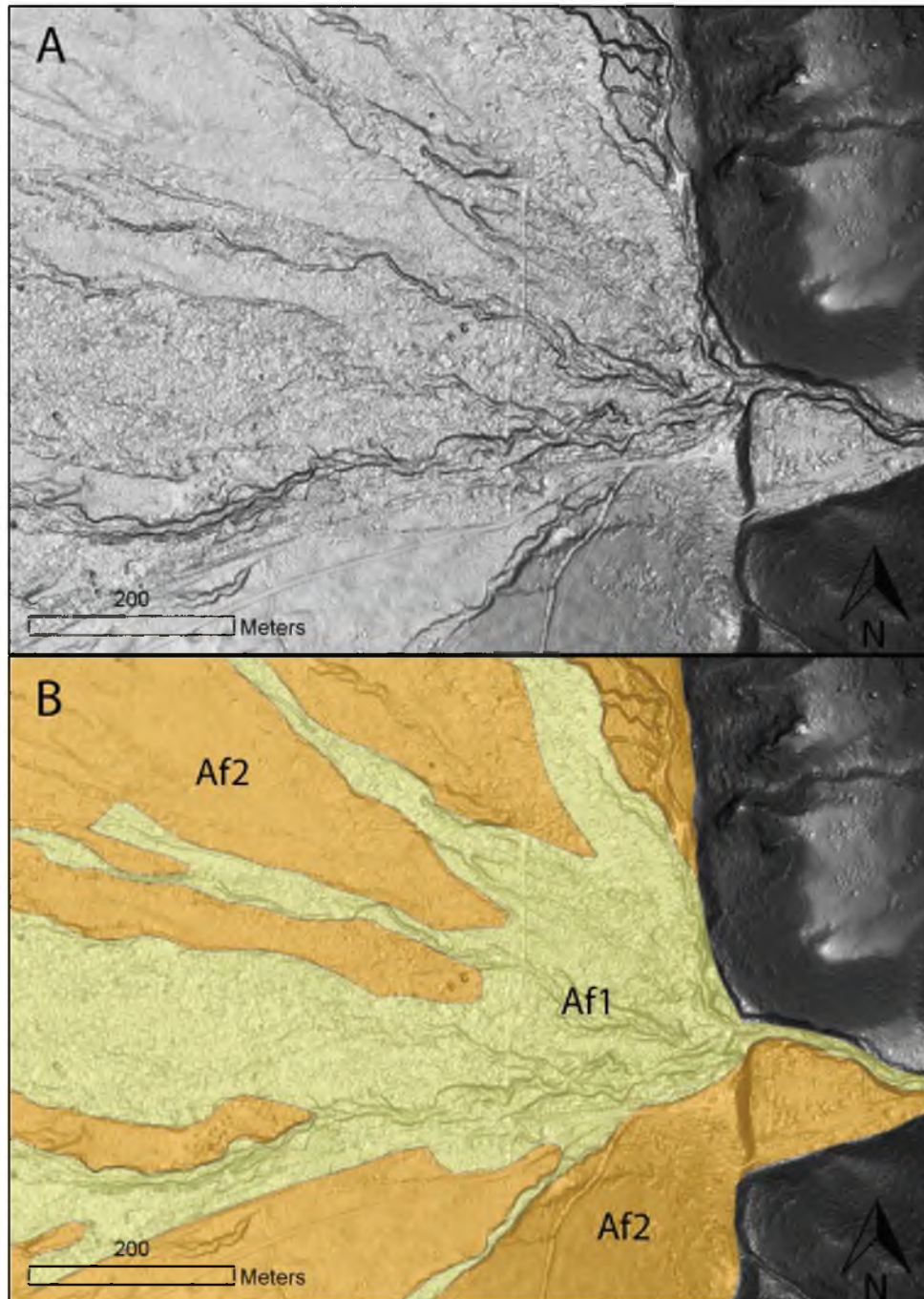
Figure 5: Slopeshade map used for highlighting and mapping alluvial fans of different relative ages. A) A slopeshade map highlights surface roughness differences between alluvial fans of two different relative ages. The younger fan is relatively rough compared to the older fan. B) Af1 and Af2 alluvial fan units have been mapped over the slopeshade map to highlight the boundaries between different degrees of surface roughness.
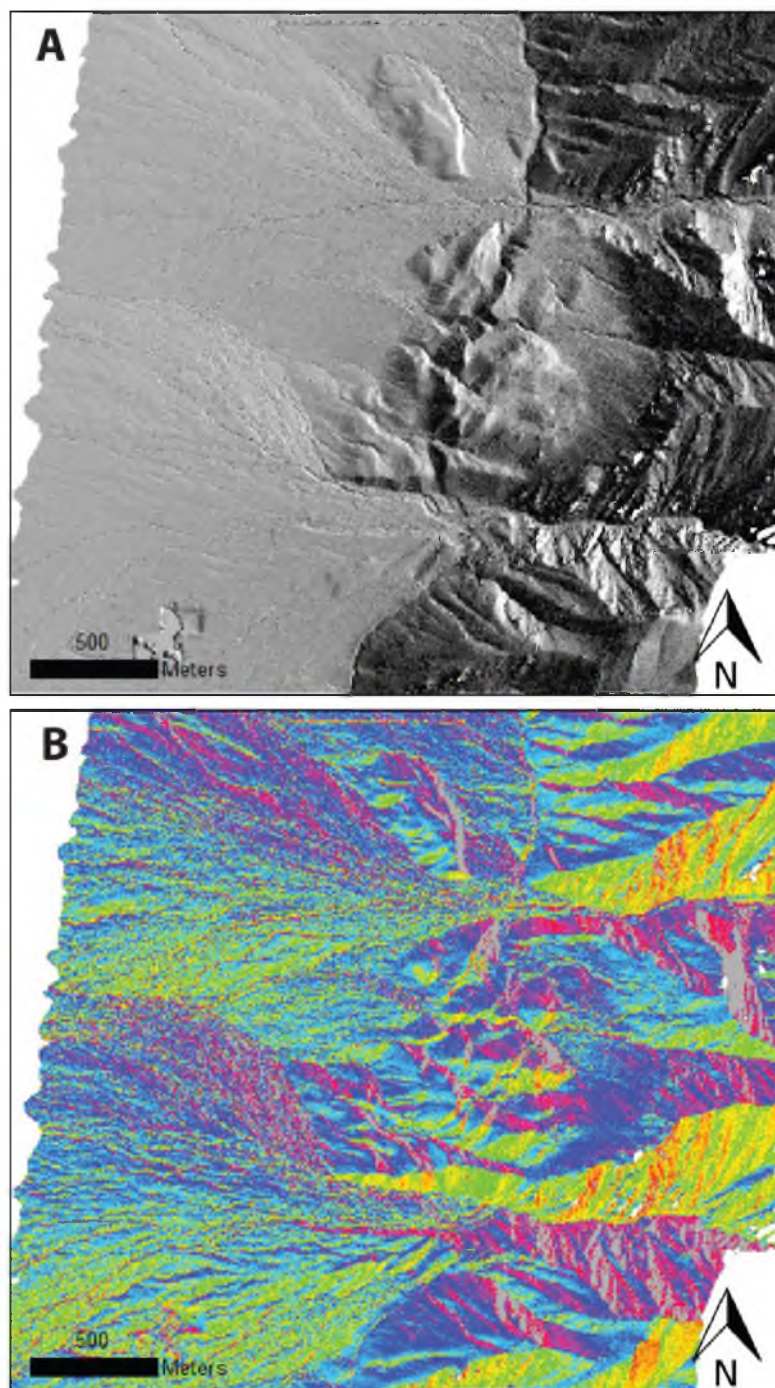
Figure 6: Comparison of A) LiDAR-derived hillshade and B) aspect map illustrating the advantages of mapping alluvial fan boundaries using aspect maps. The abrupt change in aspect along the boundary of two distinct alluvial fans is highlighted by the aspect map.
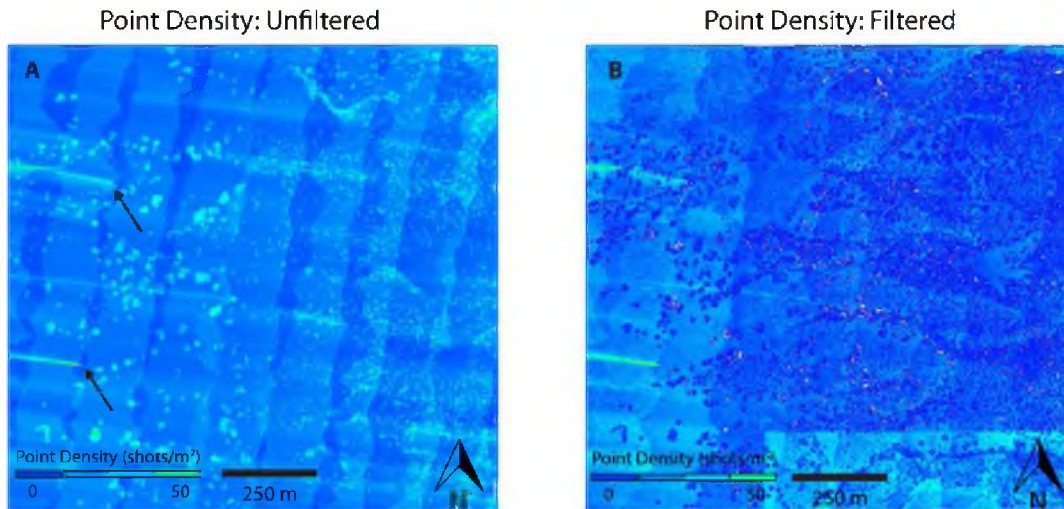
Figure 7: Point density maps of (A) unfiltered and (B) filtered LiDAR data. Vegetation occupies bright areas in the unfiltered point density map because of its high point density. In the filtered point density map, vegetation is absent and the dark spots indicate low point density. The data acquisition flight paths ran roughly north-south and irregular overlap in flight paths are most evident in the unfiltered point density map. Arrows indicate areas of high point density due to variations in the aircraft's velocity during data acquisition.

Figure 8: Hillshade map with black arrows denoting holes in the DEM caused by overly aggressive filtering of the LiDAR point cloud. The holes contain no data and therefore reflect the background color of the display screen.
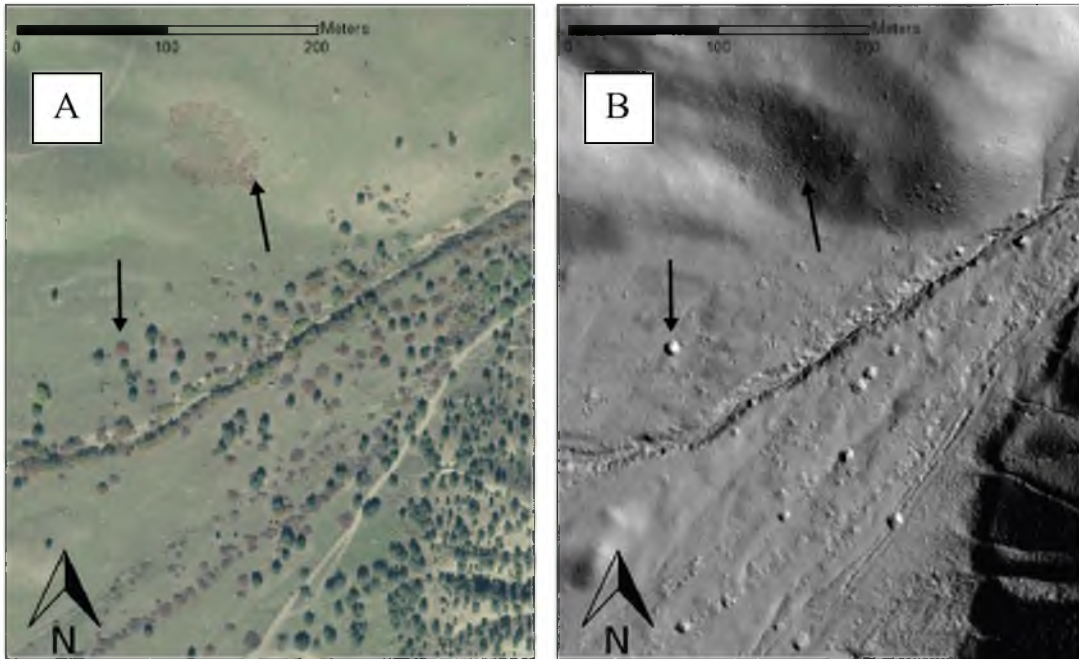
Figure 9: Comparison of vegetation features in an (A) aerial photograph and (B) hillshade map illustrating bumps, which are artifacts from inadequate filtering of vegetation reflections from LiDAR data. The left arrow indicates a bump caused by a large tree or bush. The right arrow highlights an area of small, low-lying vegetation that caused a patch of small bumps.

CHAPTER 3

DESCRIPTION OF NEPHI SEGMENT SURVEY

Survey Specifications and Quality Control

<u>Point Density</u>

Point density is defined as the number of reflections per unit area and is important

because it represents how well the ground surface is constrained within any given unit

cell. For the Nephi segment LiDAR data, UNAVCO produced DEMs gridded at a 0.5 m

posting. While this resolution may be advisable for some areas of the survey, large areas

of the survey lack a high enough point density (> 1 points per 0.25 m^2), due to leaf-on

vegetation conditions, for confidence in a 0.5 m resolution.

Using ALTM NAV planner software, UNAVCO designed the LiDAR survey to

have a point density of 6-8 points per square meter (UNAVCO, 2008) (Table 1). They

then created DEMs gridded at 0.5 m by krigging using Golden Software's Surfer 8 with a

5 m search radius for the unfiltered data and a 25 m search radius for the filtered data.

Unfiltered data contain all reflections from the LiDAR survey while filtered data contain

only ground reflections. The dataset covers 84.8 square kilometers and the unfiltered data

contain ~532,400,000 points (UNAVCO, 2008) for an average point density of 6.3 points

per m^2 or 1.6 points per 0.25 m^2. The filtered data contain ~188,500,000 points giving an

average point density of 2.2 points per m^2 or 0.6 points per 0.25 m^2.

The unfiltered data's point density of 1.6 points per 0.25 m^2 theoretically merits

gridding at 0.5 m grid resolution. However, the validity of gridding the filtered data at 0.5 m grid resolution is questionable given the average point density is less than 1 point per 0.25 m^2. Ideally, a 0.5 m gridded DEM would have a point density of at least 1 point per grid cell.

Point Density Maps

The spatial variability of vegetation cover and human or machine error during airborne LiDAR data acquisition makes the Nephi segment dataset's point density spatially heterogeneous. This means that areas of the filtered data may have a much lower point density than the average point density of 0.6 points per 0.25 m^2. I produced point density maps using the DEM generation tool on opentopography.org with a grid resolution of 1 m and a search radius of 1 m. This produced a 1 m gridded point density map with the values representing the points per 3.14 m^2. This map was then imported into ArcGIS and the Raster Calculator tool was used to divide all values by 3.14 to produce a map showing points per square meter (Figure 10).

The point density map was filtered to show areas with a point density of at least one shot per square meter and a point density of at least one point per 0.25 m^2 (Figure 11 A, B). There is a significant area containing at least one point per square meter, but the coverage for one point per 0.25 m^2 is quite small. For example, there is little area in the northern section of the dataset that contains a point density greater than 1 pt/0.25 m^2. This calls into question the validity of the choice of a gridded cell unit of 0.5m for the DEM.

Artifacts

UNAVCO produced the Nephi segment DEMs using a kriging gridding algorithm (UNAVCO, 2008) typically used when the ground surface is poorly sampled, resulting in

large gaps in data coverage. While kriging makes it difficult, it is still possible to find areas that display artifacts caused by low point density. The ground surface model in areas of low point density appears irregular and disturbed (Figure 12). These types of artifacts are especially prevalent in drainages due to the steep surface angles, whose low point density is caused by the obliqueness of the surface to the laser pulse during data acquisition, and the dense vegetation cover.

Visual Inspection of Bare Earth DEM

The bare earth model allows for the identification of features that were previously obscured by vegetation, and which may be easily overlooked while mapping in the field. A particular example from the Nephi segment is found in North Creek Canyon (Figure 13) where a strand of the fault had not been mapped previously. On an orthophoto (Figure 13A), it is nearly impossible to locate the fault scarp beneath the dense scrub oak. However, on the LiDAR-derived hillshade (Figure 13B), the fault scarp was easily located. Having located this new fault strand on the LiDAR image, a field check was performed to confirm the presence of a fault scarp. In the dense scrub oak it was easy to walk right over the fault and not notice it. Only after locating the fault on a less vegetated surface and following it into the scrub oak was the fault located and its identification confirmed.

While the bare earth DEM allows a few previously obscure fault strands to be located, mapping of the fault trace on the bare earth DEM does not significantly differ from previous mapping of the Nephi fault segment (Harty et al., 1997; DuRoss and Bruhn, 2005). This is due to the nature and thickness of vegetation cover along the Nephi segment and the nature of the fault. The southern section has relatively little dense

vegetation cover and therefore the fault scarps are mostly exposed. The northern section contains more scrub oak and the fault is more obscured by vegetation. However, the fault is located near or at the base of the mountain and is therefore easy to locate and identify on air photos and in the field without the aid of LiDAR topography.

The bare earth DEM also allows for low relief features to be located. A previously unmapped, low relief fault strand at the north end of the Nephi segment is one example (Figure 14). This fault strand has low relief (0.5-1.5 m) and is very subtle where it extends into a farmer's field and is barely discernible in aerial photographs. The southern end of the fault scarp was located and identified when walking on the ground, but the northern end that extends into the farmer's field was very subtle and perhaps unidentifiable from the ground. However, on the LiDAR-derived hillshade the fault scarp stands out clearly.

Fault Scarp Profile Surveying

I surveyed several topographic profiles in the field using a laser range finder to assess the accuracy of the LiDAR-derived DEMs. The DEMs model the ground surface within an average standard deviation of 0.53 m (derivation of this number discussed below). This standard deviation is within the margin of measurement error (discussed below) and gives confidence in the accuracy of the DEMs for a large-scale fault scarp morphological analysis. Scarp profile survey locations were chosen to contain a representative sampling of the varying topographic complexity and vegetation cover throughout the study area. The topographic profiles extended across the fault scarp and were oriented perpendicular to the scarp strike.

The coordinates at the beginning and end of each topographic profile were

recorded using a hand-held GPS, and also marked on 1 m resolution National Agriculture

Imagery Program (NAIP) color aerial orthophotos obtained from the Utah Automated

Geographic Reference Center. Profiles were then extracted from the DEM at the same

geographic coordinates and compared to the field profiles. The match between field

surveyed and DEM-extracted profiles was evaluated by visual inspection and calculation

of the variance in elevation difference between the two profiles. There is uncertainty

introduced from various sources when calculating the variance between the profiles. The

handheld GPS unit recorded the position of the profile end points within 15 m. The

position error was reduced by locating the position of the field survey on the aerial

orthophotos to +/- ~1 m. The uncertainty in relative positioning of points, surveyed with

the laser rangefinder, is estimated at +/- 10 cm horizontally, and several centimeters

vertically given the manufacturers specifications for the instrument and geometrical

errors introduced by leveling the instrument and maintaining the stadia rod in a vertical

position. At some sites the profile trace varies more than 1 m from a straight line in order

to work around vegetation or other obstacles. Locating the position of the profile on the

DEM also introduces a small amount of uncertainty, including tens of centimeters based

on the positional accuracy of the DEM data (Table 1) and +/- ~1 m associated with

comparing locations on the orthophotos and the DEM.

Relative elevations were compared along the field and DEM-extracted profiles.

First, elevations were interpolated along the profile extracted from the DEM at each field

point. The apparent error was then calculated by subtracting the interpolated DEM

elevation and field survey value and squaring the elevation difference. The variance and

standard deviation were calculated by averaging the errors, and by taking the square root

of the variance, respectively.

The average standard deviation in elevation between field- and DEM-based points is 0.53 m for the entire sample profile set (Table 2). Some DEM-extracted and field measured profiles were very similar, while others were less so (Figure 15). Profile set #1, for example, is in an area of sparse vegetation and high point density on the bare earth model, and has a low standard deviation of 0.21 m. Some of the poorly matched profile sets are located in areas of dense vegetation with considerable scrub oak, where there is low laser point density and relatively sparse ground sampling. An interesting observation is that in areas of high-density vegetation, the LiDAR DEM projects the ground surface below the surveyed profile (Profile set #3 in Figure 15). Insufficient filtering of vegetation is presumably not the cause of this discrepancy because the ground surface should be projected at higher elevations in the DEM than the surveyed profile. One possibility is that the LiDAR survey obtained no ground reflections from the area of dense vegetation, leaving a significant gap in data coverage. Another possibility is overly aggressive filtering was applied to the data. Consequently, in the DEM creation process the krigging algorithm would sample nearby ground returns to estimate the ground surface across the data gap. If the surrounding ground surface is lower than the vegetated area (perhaps because the unvegetated areas have the tendency to collect less dust, rocks, leaves, etc. than the vegetated area), then the estimated DEM surface will be lower than the true ground surface.

While an average standard deviation of 0.53 m between field and DEM-extracted profiles gives confidence in the overall accuracy of the DEMs, care needs to be taken when assessing the accuracy of an individual fault scarp profile. The point density,

vegetation cover, and processing algorithm all need to be assessed to determine the confidence in the profile's accuracy. This can be done visually by comparing a point density map of each profile's location with vegetation shown on high-resolution aerial photographs. The processing algorithm and parameters are usually available within the data's processing report.
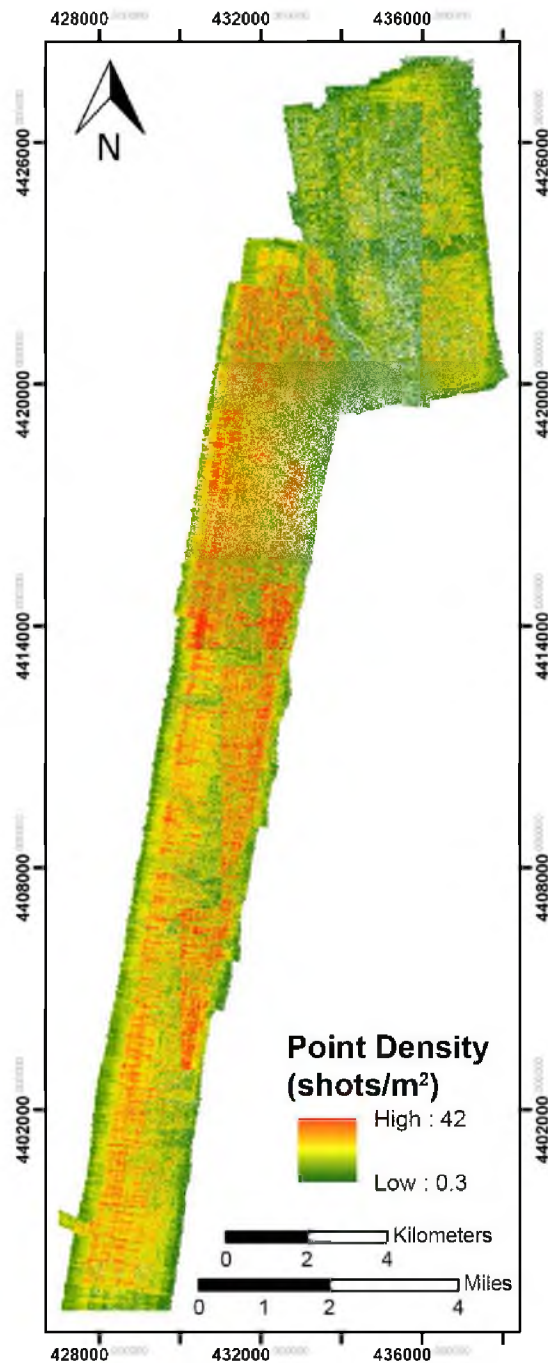
Figure 10: Point density map of the LiDAR dataset. The dataset's heterogeneity is highlighted, especially the stark contrast between point density in the northern and southern sections. Map is in UTM coordinates 12N zone.
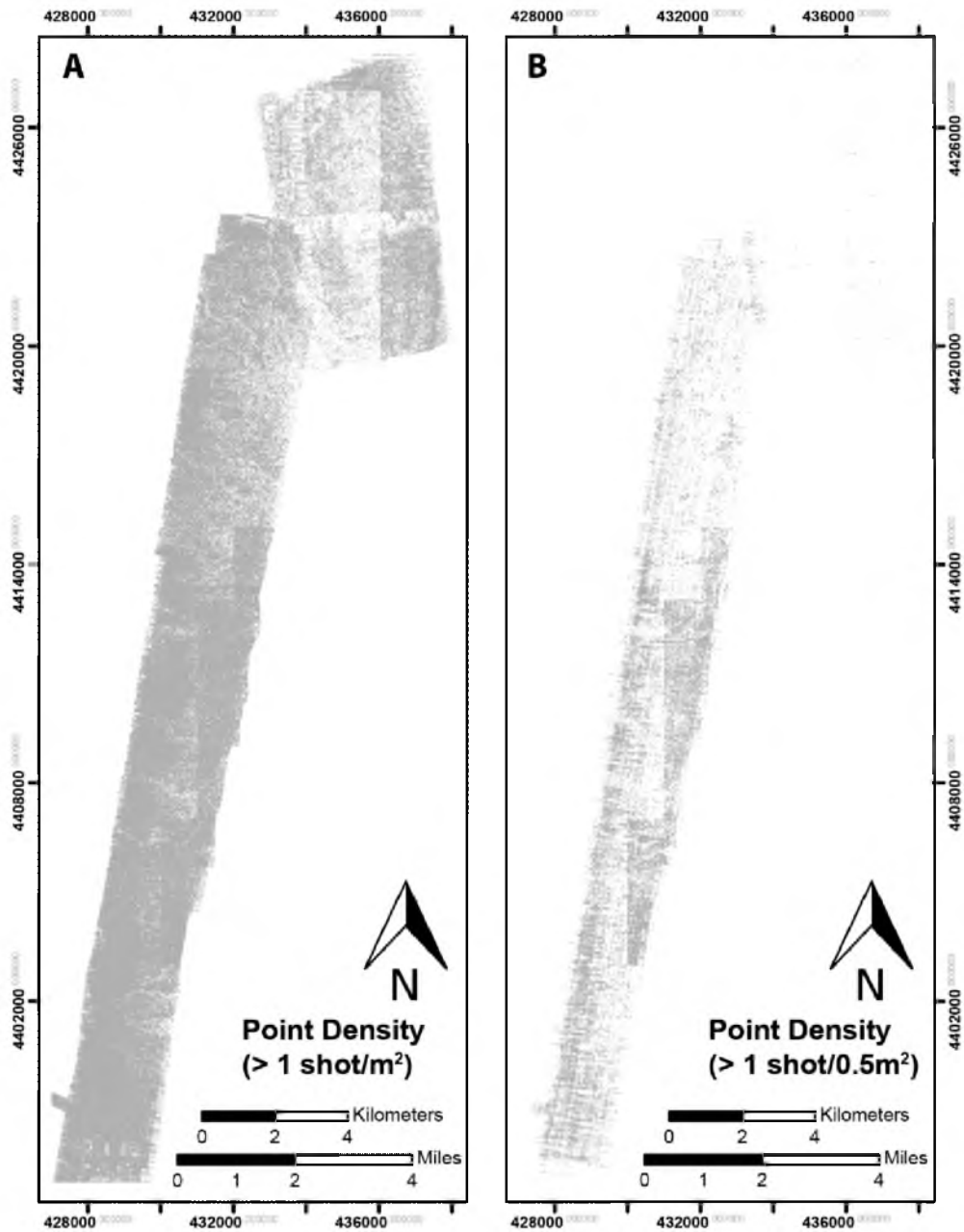
Figure 11: Point density maps of the LiDAR dataset. A) Point density map showing all areas of the survey that contain a point density greater than 1 shot/m^2. B) Point density map showing all areas of the survey that contain a shot density greater than 1 shot/0.5m^2. Maps are in UTM coordinates 12N zone.
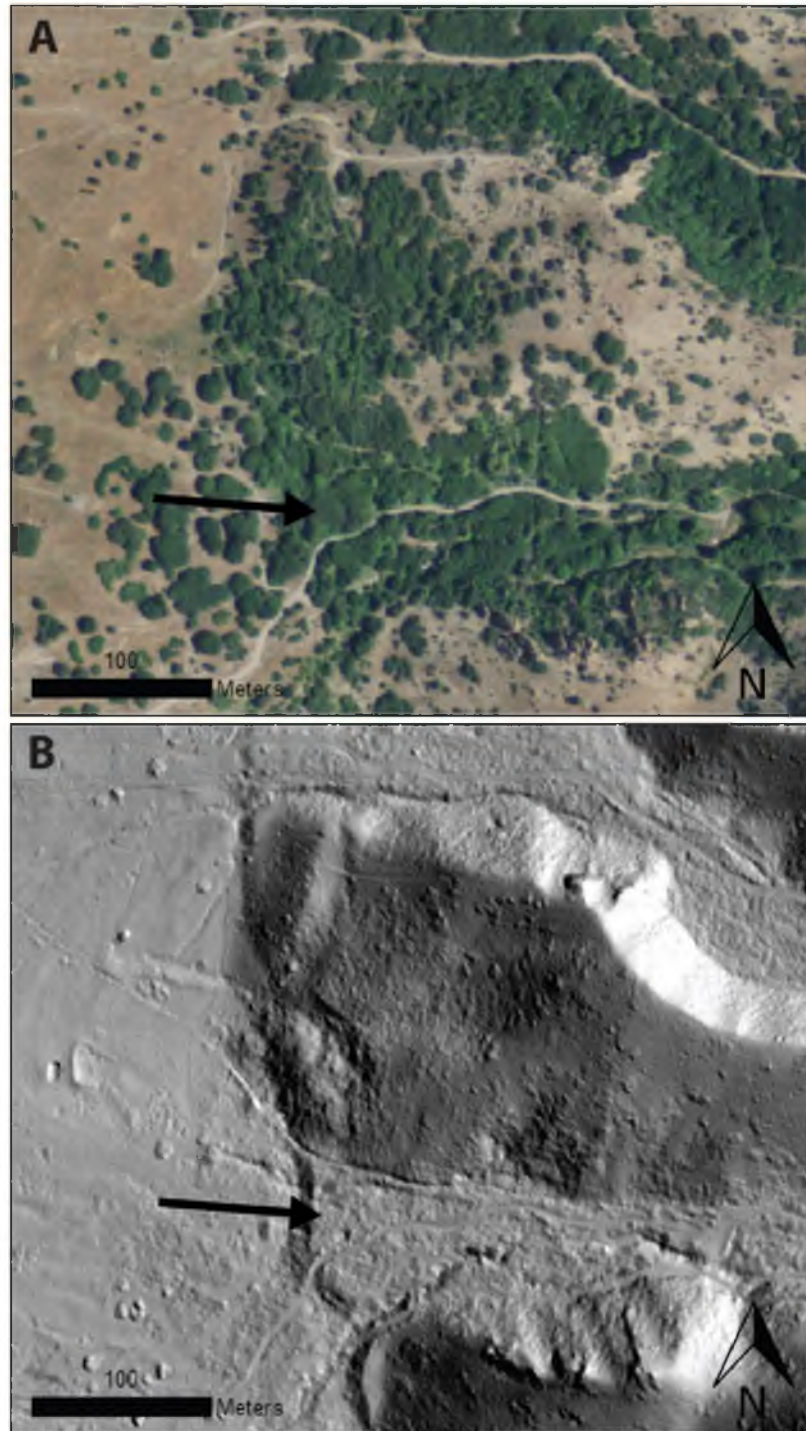
Figure 12: Aerial photograph (A) and hillshade map from LiDAR-derived bare earth model (B). The lower third (arrow indicates general area of interest) of the hillshade map displays irregular and disturbed surfaces due to imperfections in the filtering of heavy vegetation.
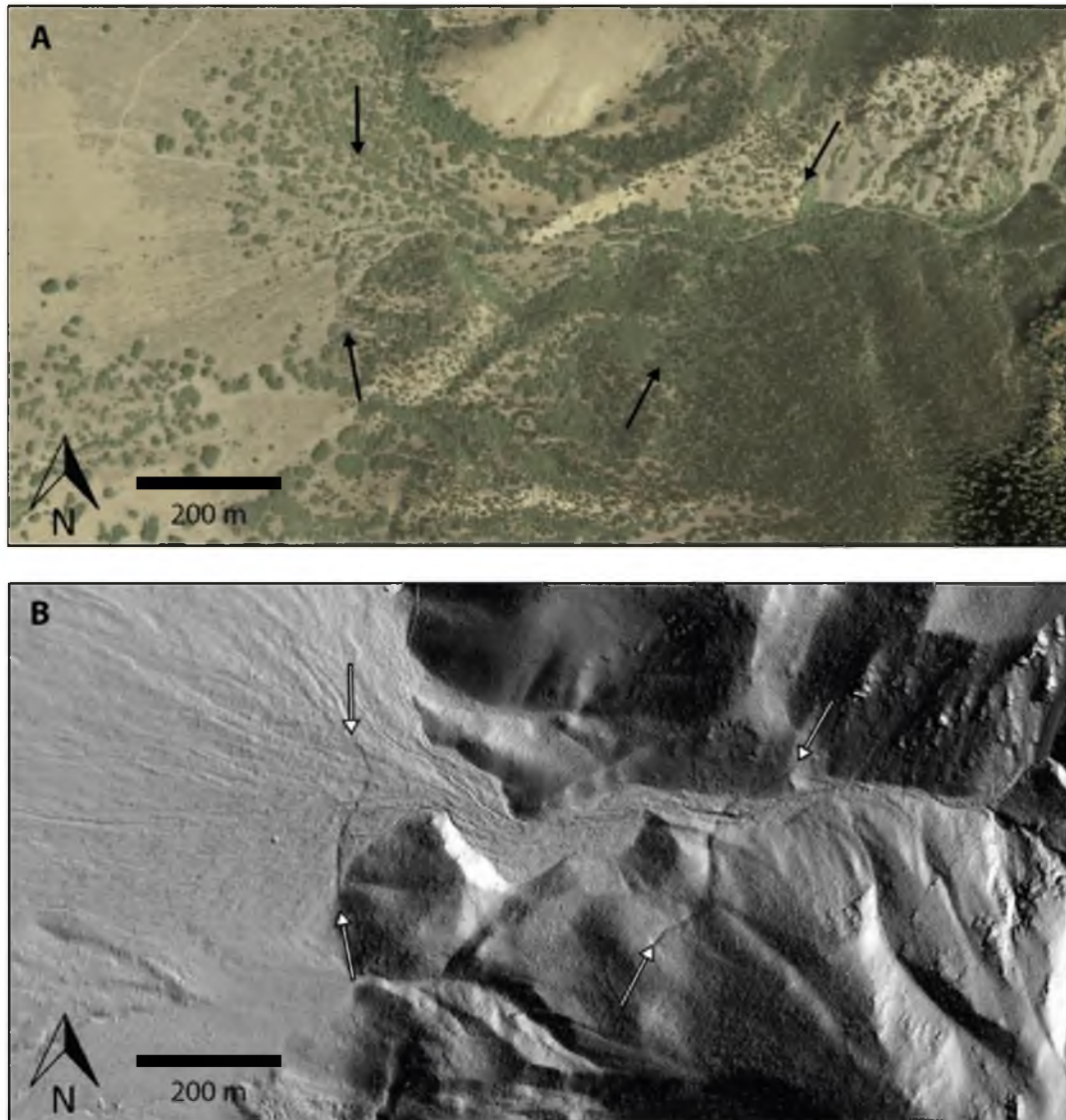
Figure 13: Comparison of fault scarp features in (A) aerial photo and (B) hillshade map from LiDAR-derived bare earth model. The fault scarp is obscured by thick vegetation in the aerial photo while the fault scarp stands out as a thin black band in the hillshade map.
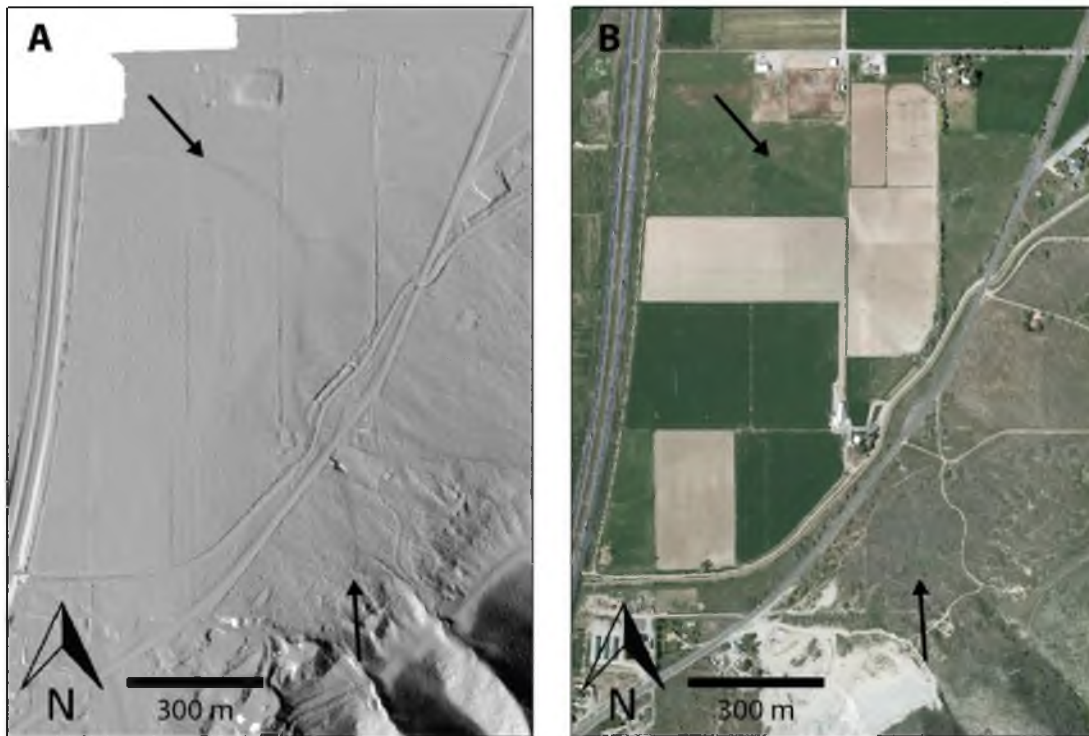
Figure 14: Comparison of low-relief (0.5-1.5m) fault scarp features in (A) hillshade map from LiDAR-derived bare earth model and (B) aerial photo. The low-relief makes the fault scarp difficult to distinguish in the aerial photo but is a well-defined darker gray band in the hillshade map.
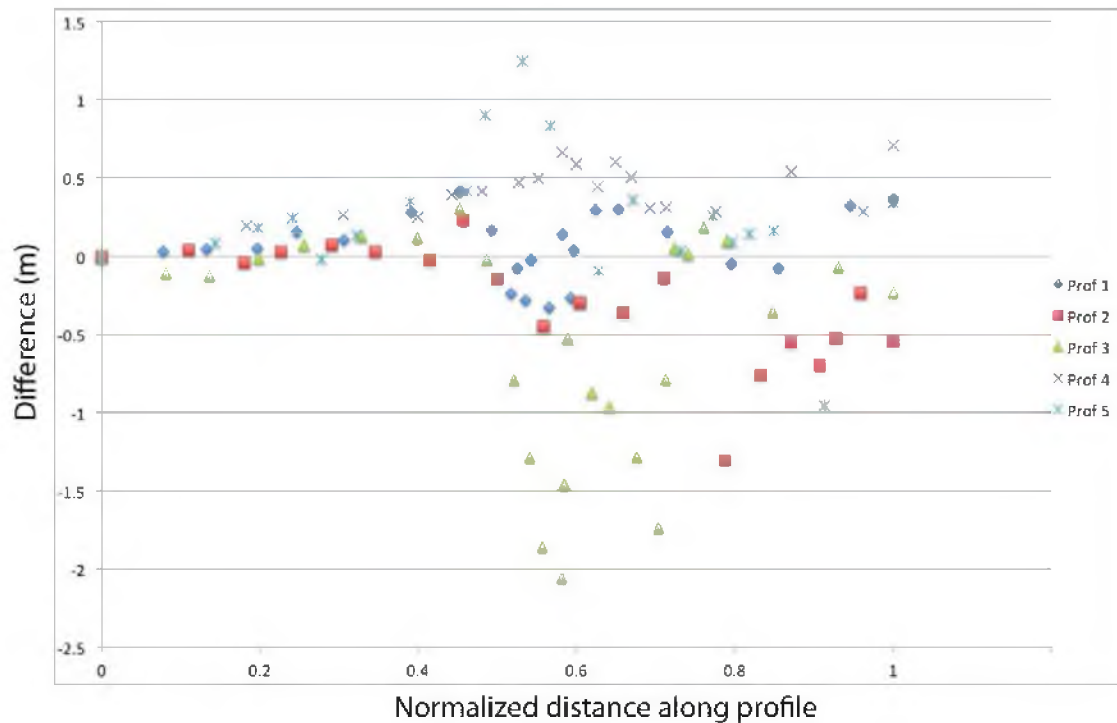
Figure 15: Differences in elevation between ground-surveyed topographic profiles and equivalent profiles extracted from the LiDAR bare earth DEM. Five profiles were surveyed perpendicular to the fault using a laser range finder. The equivalent profiles were then extracted from the bare earth DEM. The value of each equivalent point extracted from the DEM was then subtracted from the ground-surveyed point. This difference is plotted on the vertical axis with the normalized length along the profile plotted on the horizontal axis. Care was taken to extract the profile from the LiDAR at the exact position of the ground-surveyed profile. The five LiDAR-derived profiles were found to closely reproduce the ground-surveyed profiles within an average standard deviation of 0.21 m. There is a spike in difference at ~0.5 along the x-axis, most likely caused by the abrupt change in slope at the fault scarp base. Profile 3, which was the least well-fitting, experienced the greatest discrepancy of elevation differences through areas of dense vegetation.

Table 1: LiDAR Data Acquisition Details (July 9-10, 2008)

LiDAR instrumentation	Optech GEMINI Airborne Laser Terrain Mapper (ALTM)
Aircraft	Navajo Piper
Flight altitude (above terrain)	700 m
Scan frequency	70 KHz (North section) 50 KHz (South section
Scan angle	20 Degrees (North section) 15 Degrees (South section)
Overlap	50%
Planned point density	6-8 points per square meter
Elevation accuracy	5-30 cm typical $\pm$1-sigma
Horizontal accuracy	1/5,500 x altitude (m AGL) $\pm$ 1-sigma
Planning software	ALTM NAV
GPS processing software	KARS
Laser point processing software	Optech's DashMap and TerraSolid's TerraMatch
Classification and DEM production software	TerraSolid's TerraScan
DEM from ground returns	Kriging gridding algorithm / Linear Variogram
Data availability	Opentopography.org

Table 2: Field Profile/DEM Comparison

Profile	Standard Deviation (m)
1	0.22
2	0.45
3	0.85
4	0.44
5	0.49

CHAPTER 4

SOA: FAULT SCARP ANALYSIS SOFTWARE DEVELOPED

USING NEPHI SEGMENT LIDAR DATA

Background and Previous Work

With the availability of high-resolution DEMs comes a demand for software tools

to fully utilize the available data. Several software packages are available that have

varying capabilities to interact with and perform analyses on high-resolution DEMs (e.g.,

TerraScan, ArcGIS, ENVI/IDL, MATLAB, Global Mapper, GRASS, LidarViewer).

These software packages range widely in expense and capabilities (Arrowsmith et al.,

2008).

Additionally, extensions are being developed to supplement the capabilities of

these software packages to interact with and analyze LiDAR data. Software extensions

have been developed for ENVI by Nancy Glenn and others at Idaho State University

(http://code.google.com/p/bcal-lidar-tools/), for MATLAB and ArcGIS by Kelin Whipple

and others at Arizona State University

(http://www.geomorphtools.org/Tools/StPro/StPro.htm) and for MATLAB by George

Hilley at Stanford (Arrowsmith et al., 2008). These extensions add functions for LiDAR

point cloud processing, stream profile extraction and analysis, and DEM analysis.

Software extensions for fault-offset analysis are few to date. LaDiCaoz, a

software extension to MATLAB, was developed by Zielke (2009) to calculate lateral

displacement of offset geomorphic features. The development of this software was motivated by the need to measure lateral offsets on the San Andreas Fault using high-resolution LiDAR data (Zielke, 2009).

Motivation for SOA: A New Software Tool

The Nephi segment LiDAR dataset is excellent for studying normal fault offset characteristics, but sophisticated software applications for geomorphic analysis of scarps and associated features are limited. This motivated development of SOA, a custom software application for detailed geomorphic analysis of normal fault scarps.

Fault Scarp Terminology

Wallace (1977) defined much of the terminology used by paleoseismologists to describe and measure the morphology of fault scarps (Figure 16). The surface that is offset by faulting is divided into upper and lower segments located on the hanging and footwall of the normal fault. The base and crest of the scarp are defined as the lower and upper limits of the fault scarp whilst the free face is the exposed surface that results from a faulting event. The debris slope is the surface of the talus that accumulates below the free face as time progresses. The wash slope is defined as those portions of the scarp dominated by erosion or deposition. If multiple displacements occur along a fault, a composite scarp may form if the offset is localized along one or more fault strands. Also, the lower segment of the offset surface may become disrupted by antithetic faulting, forming a graben along the base of the fault scarp.

SOA was designed to analyze elevation profiles of scarps using the following paleoseismic parameters as defined by McCalpin (2009) (Figure 17).

- Base – Point of maximum topographic curvature (concave-up) between the steepest part of the scarp face and the scarp toe.

- Crest – Point of maximum topographic curvature (convex-up) between the scarp head and the steepest part of the scarp.

- Maximum slope – Gradient of the steepest part of the fault scarp.

- Far-field slope – Gradient of the faulted geomorphic surface.

- Surface offset – Vertical separation between the projections of the original upthrown and downthrown geomorphic surface.

These parameters are useful in paleoseismic investigations because they provide the means to measure surface offset and age of faulting based on diffusive erosional models of scarp degradation (Andrews and Bucknam, 1987). This information is also critical for determining slip rates, recurrence intervals, and earthquake magnitudes.

GIS Application Requirements

Fault scarp analyses are achieved by using a combination of Esri ArcGIS and custom Python scripts written by the author as part of this thesis (Appendix). The Python scripts are written so they may be operated independently of any specific GIS program to allow for their use with several different GIS applications. A GIS application is used to view and manipulate the DEM, map the fault trace, and extract elevation profiles. If a GIS application can perform the following tasks, it is compatible with the Python scripts.

1. Load and display the DEM and create hillshade maps for viewing.

2. Allow the operator to digitize a fault trace by drawing polylines.

3. Import a text (.txt or .csv) file containing lists of beginning and ending x and y coordinates and covert those into polylines. This allows a list of predefined

lines (e.g., topographic profile transects), expressed by an x and y coordinate

for each end of the line, to be quickly imported into the GIS application.

4. Extract elevation profiles from polylines with a specified point spacing (the

spacing of the DEM gridded cell) and export those profiles as a text (.txt or

.csv) file.

5. Assign attributes of a polygon or polyline to profile points if they fall within

the polygon or on the polyline (this is helpful but not crucial). This allows

extra input to limit the search for parameters within a defined window. For

example, if the crest of a scarp can be visually mapped, then the program can

limit its search for a scarp crest to within 5 m of the visually mapped crest.

Operational Procedures

The following section describes the workflow required to perform a scarp analysis

(Figure 18).

As Step 1, map the scarp base. Load and display a DEM and create a hillshade

map using the GIS application. Identify and then map the fault trace by drawing a

polyline along the base of the scarp. The fault trace does not need to be continuous. If

antithetic or multiple fault traces are present they can all be mapped. However, SOA

lacks the ability to treat antithetic or multiple fault traces individually. Care needs to be

taken to carefully follow the bends and turns of the scarp closely. For a 0.5-m DEM,

mapping at a scale of 1:1,500 will generally suffice.

As Step 2, map the crest of the scarp. Draw a polyline along the crest of the scarp

where it is discernable. If the crest is not discernable in an adjacent area, discontinue the

polyline until the crest is clearly displayed along strike.

As Step 3, map reliable areas of far-field slope. Surfaces of upper far-field slopes are mapped by enclosing them in polygons. Alluvial channels and other features can be included in the polygons. Reliable far-field slopes are often located on the footwall where surfaces of alluvial fans extend above the fault scarp. Far-field slopes are considered reliable when they are fairly smooth and continuous areas of relatively constant surface slope. Such areas are rather sparse along the Nephi segment because the fault scarp is located next to the mountain front along much of the fault trace. After the upper far-field slopes are mapped, areas of reliable lower far-field slope are mapped on the hanging wall below the upper far-field slope polygons. A column is added to the attribute table of the far-field slope polygons to record whether they are upper far-field slopes (assigned value of 1) or lower far-field slopes (assigned value of 2) and those values are later joined spatially with the extracted fault scarp profiles along with the location of the mapped crest.

Step 4 requires converting polylines into points. Each polyline must be turned into a series of points, at the desired profile spacing, with corresponding x,y coordinates, or easting, and northing coordinates in a geographic reference frame. This is accomplished in ArcGIS by first using the 'densify' tool to add vertices to the polyline at the desired point spacing. The vertices are then converted to points using the 'vertices to points' tool. These points are then given geographic coordinates by using the add xy coordinates tool.

As Step 5, export points as a .txt or .csv file.

As Step 6, run the Python script line_maker.py. Data input includes the filename (the .txt or .csv file created in Step 5), header values (ID #, x-coordinate, y-coordinate) a filename for results, and desired length (in map units) of each topographic profile. The

purpose of line_maker.py is to import the fault .txt file and to compute profiles perpendicular to the fault for the scarp analysis. The perpendicular direction at each profile location is calculated by first defining a line segment with beginning and ending points on either side of the location where the profile crosses the fault scarp. The direction of the profile is then defined as the perpendicular direction to this line segment. The program then computes a starting x,y coordinate and an ending x,y coordinate for the profile. This information is compiled into a .txt file for import into the GIS application.

For Step 7, import the .txt file created by the line_maker.py script into the GIS application. In ArcGIS, the XY_to_line tool reads the .txt file and, using the beginning and ending x,y coordinates, converts the input into polylines that represent the geographical locations of the elevation profiles to be extracted for morphological analysis.

As Step 8, convert elevation profile polylines to points. Before this step is performed, the operator may need to perform a smoothing operation on the DEM. Details for the necessity and execution of this process are outlined in Step 12. The conversion of the polylines is accomplished using the same steps used on the fault polyline outlined in Step 4 with one difference: The horizontal gridding distance of the DEM is the value to be used when specifying the vertices spacing on the line.

As Step 9, spatially join mapped crest and far-field slope information to elevation profile points. The mapped crest can be spatially joined in ArcGIS by using the join tool. This creates a new field in the elevation profile points attribute table. If any point is within a designated distance of the mapped crest polyline it will be assigned the numeric value of the crest polyline. The process is similar for the far-field slope information

except that the elevation profile points are assigned the numeric value of the far-field slope polygon if it lies within the boundaries of the polygon.

As Step 10, export the elevation profile data as a .txt or .csv file. This file includes columns recording the x, y, and z coordinates of the profile points, a reference to identify which profile the point belongs to, a reference for which points lie within the upper far-field slope polygons, a reference for which points lie within the lower far-field slope polygons, and a reference to which point lies closest to the mapped crest.

For Step 11, run the Python script separator.py. The data input for this script is the filename of the .txt or .csv file created in Step 10. At this point the input file contains a complete list of points from all of the topographic profiles for analysis. The separator.py script separates the data for each individual profile into a distinct, numbered file. The script also converts the 3D profile data into a 2D profile containing only a vertical and horizontal component. This converted 2D profile is also written to its own distinct, numbered file.

As Step 12, run the Python script soa.py. The data inputs for this script are the path and name of the folder containing all the individual topographic profile files, the number of topographic profiles to be analyzed, and the file extension of the folder where results will be saved. The scarp analyzer loads a profile's data and calculates the first and second derivative along the profile using numerical differentiation. The first derivative is calculated using a centered finite difference approximation:

$$f'x = \frac{f(x+h) - f(x-h)}{2h} \tag{1}$$

The definition of the variables is as follows:

f(x) – elevation at location x along the profile

x – horizontal position along the profile

h – horizontal distance between profile data points

The second derivative is estimated by the following equation:

$$f''x = \frac{f(x+h) - 2f(x) + f(x-h)}{h^2}$$ (2)

The base and crest of the scarp are located using the second derivative to locate positions of maximum and minimum curvature along the topographic profile. The far-field slopes should ideally be constant so there will be no change in slope as the program moves along the profile. Where the scarp begins, the second derivative should deviate from zero as slope starts to increase. The base is defined as the point of maximum slope curvature (concave-up) between the steepest part of the scarp face and the scarp toe. Therefore, it can be found as the peak of the second derivative (Figure 19). The search for the peak in the second derivative is limited to 5 m either side of the mapped fault to avoid choosing a false maximum caused by irregular topography above or below the fault scarp. The crest is found in the same way except that it is found as the minimum of the second derivative (Figure 19). The search for the crest is limited to 5 m either side of the mapped crest if it was mapped. Otherwise, it is limited to the uphill side of the scarp from the base.

Differentiation of the topographic profiles to find the slope and curvature is hindered by fluctuations in elevations created by local roughness of the ground surface and noise created by error in measurements. These fluctuations have an especially severe effect on the calculation of curvature. This causes the results to fluctuate drastically over a small horizontal distance and in some cases masks the locations of maximum and minimum curvature at the crest and base of the fault scarp (Figure 20). This problem is

mostly overcome by smoothing the profile data using a moving average filter passed over the DEM before the topographic profiles are extracted. The dimensions of the moving average filter to achieve the desired smoothing will vary depending on the DEM characteristics but a 10 unit cell X 10 unit cell will generally suffice. This can be done in ESRI ArcGIS using the focal statistics tools. The original DEM is used as the input raster and then a neighborhood (unit cell shape and size over which to average) is chosen. A variety of statistics types can be chosen but for this application the mean option is utilized. The focal statistics tool produces a smoothed DEM by calculating a value for each cell based on the mean of all the values within the neighborhood. The new DEM will exhibit smoothed topography but will still be gridded at the resolution of the original DEM.

The maximum of the first derivative is used to define the location and magnitude of the maximum slope of the scarp (Figure 19). The script limits its search for a peak in the first derivative within the bounds of the calculated crest and base to ensure that the peak truly represents the maximum scarp slope. If the search was not limited this way, steep slopes found along washes, road-cuts, or cliff-like features could be mistakenly chosen.

The next step is to determine the upper and lower far-field slopes. The script extracts the data points associated with the mapped far-field polygons and calculates best fit lines to represent the upper and lower far-field slopes. If no acceptable far-field slopes were mapped for the profile, this step is skipped. The slopes of the upper and lower far-field slopes are compared and if they are within five degrees of one another both slopes are used in the measurement of surface offset. If the difference in slopes is greater than

five degrees, only the upper far-field slope is used in the measurement of surface offset.

If the upper far-field slope is greater than ten degrees, surface offset is measured from a

horizontal datum drawn from the crest of the scarp. Ten degrees was chosen based on the

average slope of alluvial fan units offset along the Nephi segment. This parameter can be

adjusted according to the nature of the offset features of interest.

Surface offset is measured by projecting the upper and lower far-field slopes

across a vertical line drawn through the maximum slope of the scarp. However, in the

case that only the top far-field slope or a horizontal line from the crest is used, the

measurement is taken vertically from the projected line to the point of maximum slope on

the scarp and is then doubled for an estimate of surface offset. This latter approach is less

desirable than measuring the vertical distance between the projected far-field slope lines,

but is needed where grabens are located along the base of the fault scarp, or where the

lower surface was buried by younger deposits. This approach can cause abnormally large

scarp heights across grabens. If faulting has migrated towards the base of the scarp over

time, the maximum slope of the scarp may be located low on the scarp rather than near

the center. This situation must be recognized by visual inspection of profiles because

automated calculations will overestimate the surface offset. This process could be

automated by flagging scarp offsets in which the maximum slope does not lie within a

predetermined, normalized distance from the center of the scarp.

The data from the measurements are recorded to three separate text (*.txt) files.

The base.txt file contains the ID number and the x, y, and z coordinates of the scarp base

location for each profile. The crest.txt file contains the ID number and the x, y, and z

coordinates of the scarp crest location for each profile. The slope.txt file contains the ID

number, and the x, y, and z coordinates of the point of maximum scarp slope, the

magnitude of the maximum slope, the magnitude of surface offset, and a numeric key

indicating the method used to measure surface offset.

As Step 13, run the Python script stem_plotter.py. The stem_plotter.py script

converts the surface offset measurements into a format useful for visualization in GIS

applications (Figure 21). The script runs following input of the filename of the slope.txt

file created in Step 12, and new filename for the output created by the script. Each

surface offset measurement is converted into a line with length proportional to the

measured offset. The line's initial point is located at the base of the scarp and the line is

projected outward perpendicular to scarp strike.

For Step 14, visually inspect data for errors. The files created in Step 13 are

imported into a GIS application to visualize the locations of the base, crest, and

maximum slope of the fault scarp. Although optional, this step is important to ensure the

program picked appropriate locations for each parameter (Figure 21). Areas of obvious

error in picking locations of scarp base, crest, and maximum slope can either be excluded

by editing or the program can run again using refined parameters to gain a better fit.

Experience shows that the soa.py script may incorrectly pick the base, crest, and

maximum slope locations where the mapped scarp crosses washes, where there is

complicated topography directly above or below the scarp, or where the scarp has

undergone anthropogenic alteration. The stem plots of surface offset created in Step 13

can also be imported for visual inspection of variability and consistency in vertical

displacement (Figure 21). Unusually large or small offset measurements can be excluded

by editing the data files. Significant errors in offset measurement are caused by the

factors that create errors in locating the base, crest, and maximum slope locations on scarp profiles. Other errors in surface offset measurement may occur if the script calculated incorrect far-field slopes.

Software Limitations/ Needs for improvement

SOA has limitations that must be considered when performing a scarp morphological analysis. Currently, the software does not have the capability to recognize and correctly adjust offset measurements where the profile crosses grabens created by antithetic faulting. Along strike step overs between fault segments are also not accommodated and must be accounted for by visual inspection to ensure that each fault segment is treated independently. SOA also does not have the capability to recognize, measure, and combine offsets when multiple faults are crossed by a single topographic profile. Lastly, there are problems related to calculating offset where the maximum slope angle is located near the base rather than the center of the scarp, and where there is no reliable lower far-field slope. These limitations need to be kept in mind when assessing the quality of and manually filtering offset measurements produced by the software. Further work is needed to improve the capabilities of the software to recognize and correctly deal with varying types of scarp features.
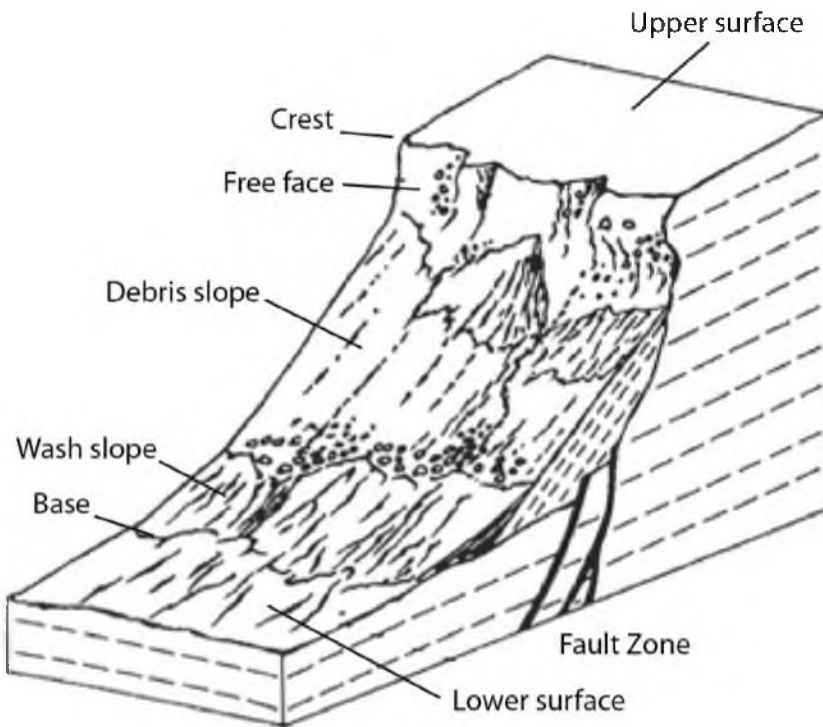
Figure 16: Illustration of a normal-displacement fault scarp shortly after an earthquake with its associated terminology. In this example, the free face has not yet been modified by erosion and partly buried by deposition. Modified from Wallace (1997).
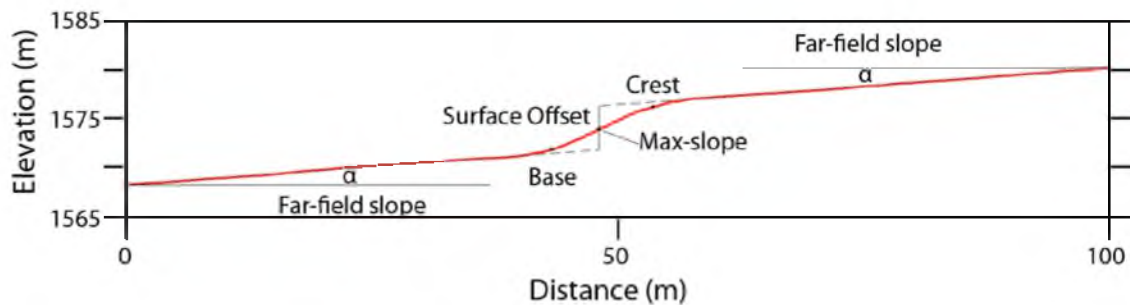
Figure 17: Fault scarp topographic profile illustrating the relative positions and names of geomorphic features used in analysis of scarp offset and slope angle. Modified from McCalpin (2009).

Step 1: Map the scarp

Step 2: Map the crest of the scarp

Step 3: Map reliable areas of far-field slope

Step 4: Convert the polyline into points

Step 5: Export points as a .txt or .csv file

.txt or .csv file from Step 5

Step 6: Run the python script line_maker.py

output file from Step 5

Step 7: Import the .txt file created by the line_maker.py script into the GIS application

Step 8: Convert elevation profile polylines to points

Step 9: Spatially join mapped crest and far-field slope information to elevation profile points

Step 10: Export the elevation profile data as a .txt or .csv file

.txt or .csv file from Step 10

Step 11: Run the python script seperator.py

Step 12: Run the python script scarp_offset_analyzer.py

Step 13: Run the python script stem_plotter.py

output file from Steps 12 & 13

Step 14: Visually inspect data for errors

Figure 18: Work flow diagram illustrating the steps necessary to perform the scarp morphological analysis using a combination of GIS software and SOA python scripts. Square boxes on the left are steps carried out in a GIS application. Ellipses in the center represent input and output files. Rounded boxes on the right represent the Python scripts to be executed.
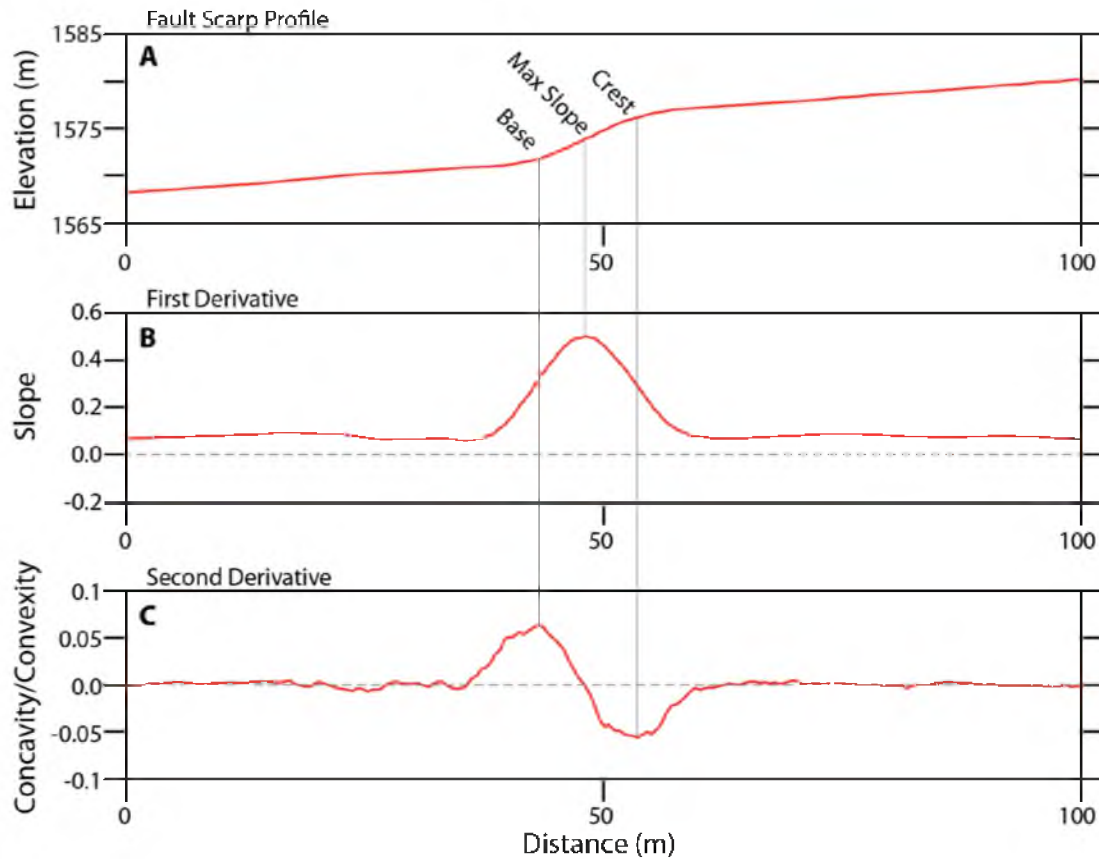
Figure 19: A fault scarp profile (A) with plots of the profiles numeric first (B) and second (C) derivative. The maximum slope is located at the peak position of the first derivative. The base and crest of the scarp are located at the maximum and minimum positions of the second derivative, respectively.
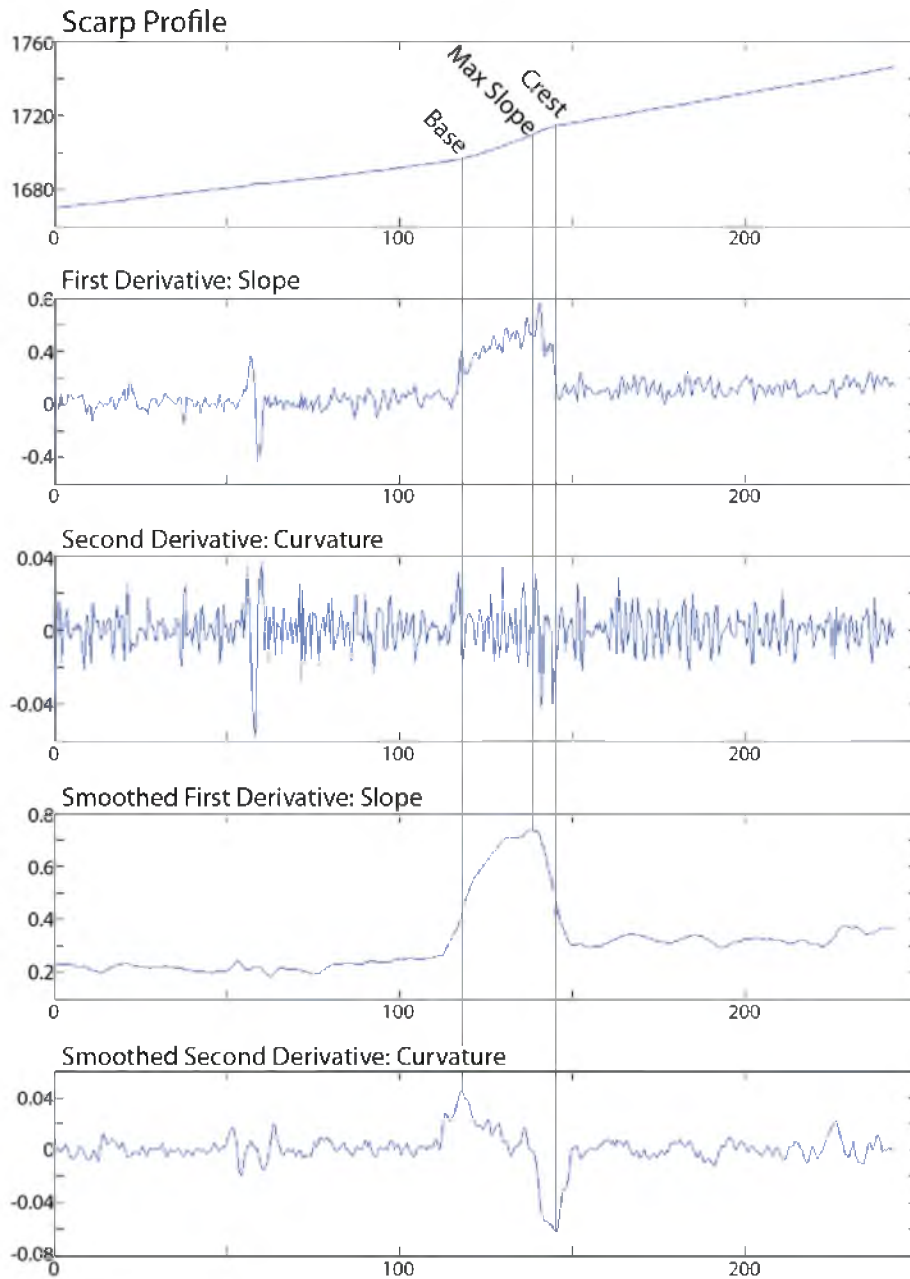
Figure 20: A graphical illustration of data processing to remove noise by running averaging of DEM data. The example shows a topographic profile extracted from the full-resolution DEM (0.5 m horizontal posting) with raw first (B) and second (C) derivatives followed by the same derivatives calculated from the smoothed DEM (D and E). See text for further discussion of averaging filter.
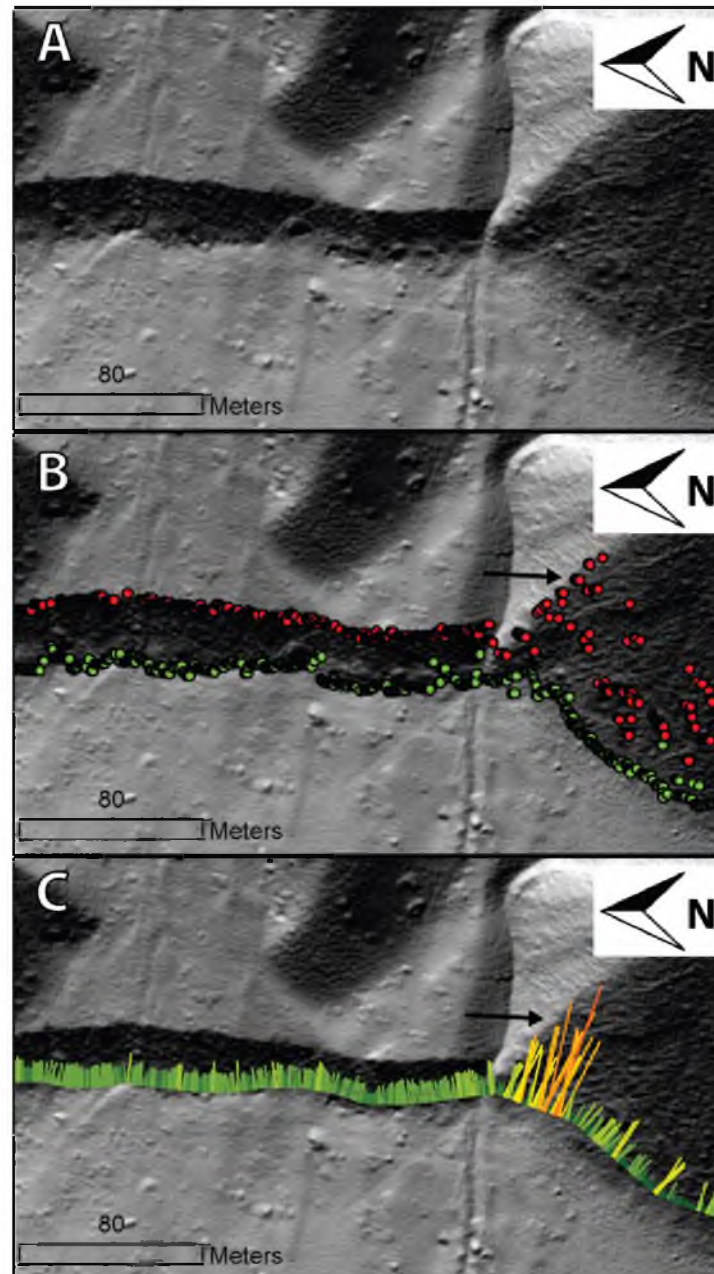
Figure 21: A) Hillshade map, B) hillshade map overlain with mapped crest (red dots) and base (green dots), and C) hillshade map overlain with stem plots of surface offset. Arrows indicate areas with erroneous offset values, resulting from uncertainty in the scarp crest location that must be rejected. The red and green dots represent base and crest positions picked by the Python script scarp_offset_analyzer.py.

CHAPTER 5

APPLICATION - NEPHI SEGMENT OF THE WASATCH FAULT

Previous Work

The Nephi segment has undergone a wide range of studies including surface

geology mapping (Harty et al., 1997), fault scarp profiling (DuRoss and Bruhn, 2005),

fault scarp diffusion modeling (Mattson and Bruhn, 2001; DuRoss and Bruhn, 2005), and

paleoseismic fault scarp trenching investigations (Hanson et al., 1981; Jackson, 1991;

Machette et al., 2007; DuRoss et al., 2008). This work has been conducted to determine

the chronology and magnitude of faulting events along with associated slip rates. These

studies provide information useful for validating the results of surface offset

measurements and for interpreting overall trends in surface offset along the fault.

Alluvial Fan Deposits

The Nephi segment of the Wasatch fault offsets four main alluvial fan units: af1

(upper Holocene), af2 (middle Holocene to uppermost Pleistocene), afb (uppermost

Pleistocene related to the Bonneville phase of the Bonneville lake cycle), and afo (upper

to middle Pleistocene; pre-Bonneville lake cycle) (Harty et al., 1997). The af1 unit is

characterized by irregular fan surfaces, with well defined debris flow channels and levees

(DuRoss, 2004). The af2 unit is characterized by smoother fan surfaces with minor

irregularities, 3-4 m of stream incision, and each fan occupies ~2-4 km^2 in the southern

strand and ~1-2 km^2 in the northern strand (DuRoss, 2004). The morphology of the afb

unit is similar to the af2 unit except for greater vertical incision (7-8 m) and surface offset

where cut by the fault (DuRoss, 2004). The afo unit is characterized by planar surfaces

that lack debris flow levees and channels and by 10-20 m of stream incision (DuRoss,

2004).

Fault Scarp Diffusion Modeling

Mattson and Bruhn (2001) performed fault scarp diffusion modeling on three

scarps of increasing age to determine short- and long-term slip rates at Red Canyon, near

the southern end of the Nephi segment. They report slip rates of 1.3 mm/yr, 0.6 mm/yr,

and 0.4 mm/yr for the youngest (4.3 ka initiation), intermediate (35 ka initiation), and

oldest (70 ka initiation) fault scarp, respectively. Mattson and Bruhn (2001) suggest that

the variable slip rates found for units of different age are evidence for either temporal

clustering of earthquakes or temporal variations in slip rate along the Nephi segment.

DuRoss and Bruhn (2005) utilized the geometry and extent of surface faulting,

fault scarp diffusion modeling, and paleoseismic trenching data to constrain long- (late

Pleistocene) and short-term (Holocene) slip rates and recurrence intervals. They first

defined a preferred rupture scenario based on scarp diffusion modeling and paleoseismic

data. Using the preferred rupture scenario they determined a recurrence interval of 1.6

kyr since the mid-Holocene (~7 ka), 5.4 kyr from the mid-Holocene (~ 7 ka) to latest

Pleistocene (~12 ka), and ~9.0 kyr from the latest Pleistocene (~12 ka) to late Pleistocene

(~53 ka). DuRoss and Bruhn (2005) also determined slip rates for the aforementioned

time periods of 0.5-0.7 mm/yr, 0.3-0.4 mm/yr, and 0.2 mm/yr, respectively. DuRoss and

Bruhn (2005) also draw attention to the increased frequency of earthquakes in the

Holocene on the Nephi segment as an indicator of possible temporal clustering of earthquakes. They also cite evidence that the northern and southern fault strands may behave independently.

Paleoseismic Trenching Investigations

Paleoseismic trench excavations performed on the southern strand of the Nephi segment at North Creek by Hanson et al. (1981) and at Red Canyon by Jackson (1991) were reviewed and a consensus on the timing of surface-faulting earthquakes was reported by the Utah Quaternary Fault Parameters Working Group (UQFPWG; Lund, 2005) for the three most recent events:

- P1: <1000 (possibly as recent as 400) cal yr B.P.

- P2: ~3900 cal yr B.P.

- P3: 3900-5300 cal yr B.P.

These paleoseismic data were considered poorly constrained and suggest multiple surface-faulting chronologies depending on which age data were accepted or rejected (Lund, 2005). DuRoss et al. (2008) pose an alternative chronology for P2 of 1300 – 1700 cal yr B.P. based on accepting and discarding different age data. Lund (2005) also determined a slip rate of 0.5–1.1–3 (minimum-preferred-maximum) mm/yr and a recurrence interval of 1.2-2.5-4.8 kyr.

Another paleoseismic trenching investigation was conducted on the southern strand of the Nephi segment at Willow Creek (Machette et al., 2007). Three surface-faulting events were identified and dated to have occurred between 300 and 2320 years B.P. A slip rate of 2.0-2.5 mm/yr was determined for the 2000 year P1-P3 interval, which is the highest published slip rate for the Nephi segment.

Trenching on the northern strand of the Nephi segment near Santaquin by DuRoss et al. (2008) found evidence for a single surface-faulting earthquake that occurred 500 +100/-150 cal yr B.P. and displaced early to mid-Holocene alluvial fan deposits 3.0 ± 0.2 m. DuRoss et al. (2008) also cited evidence that P2 occurred at least 1500 cal yr B.P. and most likely occurred 6100 – 7000 cal yr B.P. A long-term geologic vertical slip rate of 0.5 mm/yr was calculated using displaced Bonneville shorelines. This slip rate yields an average recurrence interval of 6000 ± 400 years. DuRoss et al. (2008) cite the longer recurrence interval for the northern strand and the disparate late Holocene earthquake chronologies as evidence that the two strands of the Nephi segment may behave independently.

Summary of Previous Work

Paleoseismic fault scarp trenching investigation and fault scarp diffusion modeling constrain a slip rate between 0.5 mm/yr and 3 mm/yr for the last three surface-rupturing events, while longer-term slip rates are as low as 0.2 mm/yr. Recurrence intervals for the southern segment range from <1,000 years to 4,800 years while the northern segment has a calculated recurrence interval of 6000 ± 400 years. There is evidence for possible temporal clustering of earthquakes or temporal variations in slip rate along the Nephi segment. There is also evidence that the northern and southern strands of the Nephi segment may behave independently. Offset is preserved on four main alluvial fan units: af1 (upper Holocene), af2 (middle Holocene to uppermost Pleistocene), afb (uppermost Pleistocene related to Bonneville phase of the Bonneville lake cycle), and afo (upper to middle Pleistocene; pre-Bonneville lake cycle).

Automated Scarp Profile Results

Using the steps outlined in section 4.5, profiles were extracted and analyzed every

1 m along the length of the mapped fault scarp producing 36,757 offset measurements.

The two visualization methods (inspecting the location of the scarp base, crest, and

maximum slope and comparing the vertical offset measurement to those around it)

outlined in the software section in Step 14 were used to assess the accuracy of the offset

measurements. This resulted in nearly half of the surface offset measurements being

rejected for further analysis. Suspect measurements included offsets that were

anomalously high or low compared to surrounding ones, offsets measured using a base or

crest value that was erroneous based on visual inspection, and all negative offset values.

All surface offset measurements located on landslides were also rejected due to the

possibility that some or all of displacement could be caused by mass wasting rather than

tectonic faulting. After filtering out the invalid measurements, 19,798 profiles remained

for analysis. For comparison, roughly 90 scarp profile displacement measurements have

been obtained by previous workers using ground surveying techniques (Jackson, 1991;

Machette, 1992; Harty et al., 1997; Mattson and Bruhn, 2001; DuRoss, 2004).

To test the validity of the results of the scarp analysis, I compared surface offset

measurements produced by SOA with field surveyed surface offset measurements

produced by Jackson (1991), Mattson and Bruhn (2001), and DuRoss (2004) at 17 sites

distributed along the Nephi segment data. The nearest five SOA measurements were

averaged from the location of the field survey. The difference was then calculated for

each site and a mean was calculated from the sum of the differences. The mean difference

in surface offset between the field survey and SOA measurements was found to be 21

percent (Table 3). The small mean difference between field and SOA measurements gives confidence in the accuracy of measurements produced by utilizing SOA on high-resolution LiDAR data.

Along Strike Variability in Surface Offset Adjacent to Field Surveyed Profiles

I plotted two scarp profile offset measurements: DuRoss (2004) Profile #9 and the southernmost profile of the Nephi segment of Mattson and Bruhn (2001), along with 30 scarp profile offset measurements from SOA results (15 measurements from both sides of the field surveyed profiles) (Figure 22). The DuRoss (2004) Profile #9 has a surface offset of 8.5 m. The 30 SOA offset measurements have a range from 5.4 m to 9.8 m with an average offset of 8.2 m. The Mattson and Bruhn (2001) profile has a surface offset of 6 m. The 30 SOA offset measurements have a range from 5.4 m to 6.8 m with an average offset of 6.3 m.

These results display the subjectivity of selecting a single profile along a scarp to quantify offset over scales as little as tens of meters along strike. The ability to measure and quantify the natural variability in offset is a significant advancement in technique provided by the high-resolution LiDAR dataset and SOA software.

Offset vs. Deposit Age

Offset Measurements on Alluvial Fans of Different Age Range

Surface offset measurements were assigned to four fan units defined on the 1:50,000 scale Quaternary geology map of the Nephi Fault segment (Harty et al., 1997): af1 (late Holocene), af2 (early to mid-Holocene), afb (latest Pleistocene), and afo (late Pleistocene). This produced 12, 17, and 3 distinct geographic sites for faulting of af1, af2,

and afo, respectively, because of the uneven distribution of these deposits along the length of the fault. Mean offset was calculated for each site and the results were plotted on a figure modified from Figure 19 of DuRoss (2004) showing distribution of surface offset among alluvial fan-units along the strike of the fault (Figure 23). Mean offsets for af1, af2, and afb sites determined in this study correspond well (within 1-2 m) with offset measurements reported by DuRoss (2004). In contrast, mean offsets for afo (referred to as Af3 by DuRoss, 2004) only correspond well at the southernmost site.

Standard deviations of the surface offset measurements were also calculated for each site (Figure 23). These standard deviations range from ~2 m within af1 fan units to greater than 10 m within afo fan units. This further illustrates the variability in offset along strike within fan units of similar age as noted in section 5.2.1. Furthermore, surface offsets measured on all of the fan units (af1, af2, and afo) overlap each other within one standard deviation, implying that magnitude of offset is not a reliable geomorphic metric for assigning relative age to surface units.

Part of the overlap in surface offset on fans of different age as mapped by Harty et al. (1997) is caused by the relatively small 1:50,000 mapping scale, which is insufficient to show the details of fan deposition and age along the length of the fault over distances of a few tens of meters. I attempted to improve the surficial geologic mapping by using (1) detailed field observations at ground surveyed scarp profile localities (DuRoss, 2004), (2) visual inspection of hillshade imagery, slopeshade imagery, and high-resolution (1 m) aerial photography, and (3) morphological measures of fan surfaces extracted from the LiDAR DEM. Visual inspection of hillshade and slopeshade imagery and aerial photographs proved to be most useful.

DuRoss (2004) profile data. DuRoss (2004) surveyed, analyzed, and compiled

~80 fault scarp topographic profiles within the area of the LiDAR survey. Each of these

profiles was assigned an alluvial fan unit based on morphological observations. I plotted

the profile locations on the LiDAR-derived DEM along with their assigned alluvial fan

units to better constrain age surface mapping resolution. Unfortunately, only a small

number of topographic profiles were completed on alluvial fan surfaces that were not

already assigned an alluvial fan unit from the surficial geologic map of Harty et al.

(1997). Therefore, this approach did not significantly improve the resolution of the

surficial geologic map.

Visual mapping of LiDAR imagery. Hillshade and slopeshade maps derived from

the high-resolution LiDAR data along with high-resolution aerial photographs were

utilized to map alluvial fan remnants and assign alluvial fan units. The af1 unit can be

identified in LiDAR-derived hillshade and slopeshade maps by its rough, irregular texture

(Figure 5). The af2 unit is relatively smooth, compared to af1 surfaces. It also exhibits 3-

4 m of vertical incision (Figures 5, 24). The afb unit is similar to the af2 unit except that

it has increased vertical incision (7-8 m) and vertical displacement (DuRoss, 2004). It is

very difficult to differentiate the afb and af2 units visually in LiDAR-derived hillshade

and slopeshade maps. The afo unit is characterized by planar surfaces without debris flow

levees and channels, and 10-20 m of steam incision (DuRoss, 2004) can be distinguished

in LiDAR-derived hillshade and slopeshade maps by very smooth and rounded features

(Figure 24).

This visual approach yielded limited results that did not greatly improve the

resolution of the surficial geologic map. Because the fault extends along the base of the

mountain front, only small alluvial fan remnants are typically preserved on the upthrown (east) side of the fault. These small alluvial fan remnants are numerous and occur along most of the fault trace (Figure 25). However, the small surface areas of these alluvial fan remnants make assigning an alluvial fan unit based on geomorphic observations difficult. It is also unadvisable to assign an alluvial fan unit based on the fan unit found on the adjacent hanging wall because these latter units are commonly younger due to deposition below the scarp following surface offset events. As a result, I was only able to assign the largest unmapped alluvial fan remnants (5 of the ~100 fan remnants) to a specific alluvial fan unit.

Surface roughness characterization. The relative age of an alluvial fan surface may, in some cases, be determined using surface morphology (Wells et al., 1987; Bull, 1991). For example, Frankel and Dolan (2007) and Cavalli and Marchi (2008) used high-resolution DEMs to calculate surface roughness and ultimately characterize and differentiate alluvial fan surfaces of different relative ages.

Several methods exist for calculating surface roughness, each with its own advantages and limitations (Grohmann et al., 2011). I used two methods to investigate surface roughness along the Nephi segment due to their applicability to geomorphic analysis and ease of calculation: standard deviation of slope and standard deviation of residual topography. The standard deviation of slope was calculated from a slope map using a 5-unit cell by 5-unit cell moving window (Frankel and Dolan, 2007). Standard deviation of residual topography was calculated by first calculating the difference between the original, full-resolution DEM and a smoothed DEM. For this application, the same smoothed DEM was used as was produced for the fault scarp profile analysis (see

section 4.5 Step 12). Then the standard deviation of the differences was calculated within a 5-unit cell by 5-unit cell moving window (Grohmann et al., 2011).

I was unable to map relative fan-surface ages using surface-roughness; however, this method deserves further investigation. On the Nephi segment DEMs, particularly near the fault trace, poorly filtered vegetation significantly impacts the surface-roughness calculations (Figure 26). This contribution is large enough to dominate the surface roughness signal, making distinguishing fan units of varying relative ages too difficult. This effect was seen in both methods of calculating surface roughness. These methods show potential for distinguishing between fan units where vegetation diminishes west of the fault.

Along-strike Surface Offset Variability
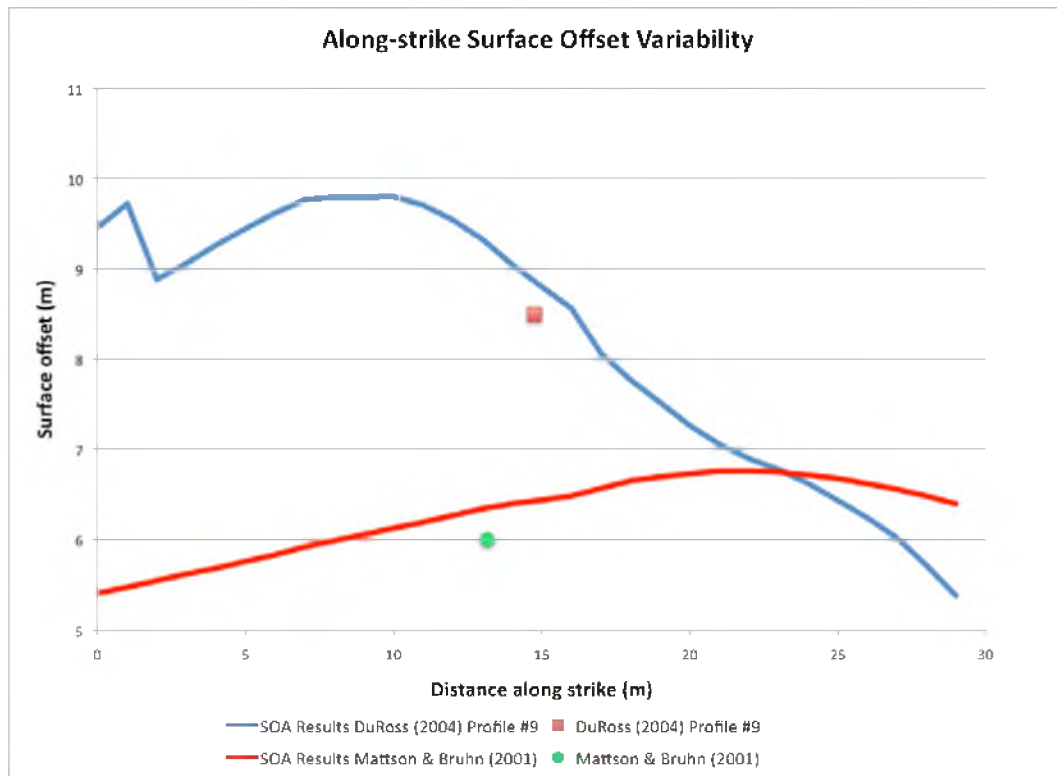
Figure 22: Along strike surface offset variability. Two surface offset measurements derived from scarp profiles from previous studies (DuRoss, 2004; Mattson and Bruhn, 2001) were plotted along with 30 offset measurements (the 15 closest measurements from either side) produced by SOA. The more detailed and continuous offset measurements of SOA display the variability in offset within a short distance along the fault. This continuous picture of offset variability allows maximum, minimum, and average offsets to be found instead of relying on a single point measurement from one profile or multiple profiles a few meters apart.
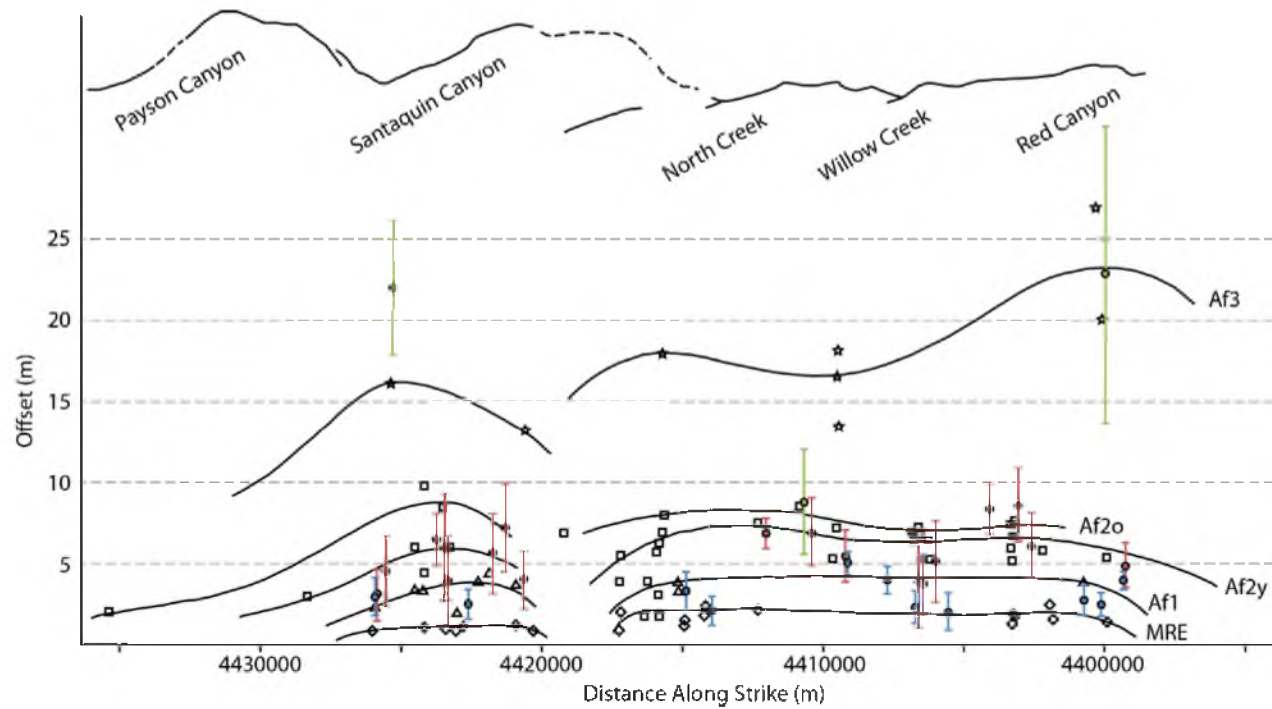
Figure 23: LiDAR-derived scarp offsets (this study) plotted on the distribution of surface offset from field surveying shown in figure from DuRoss (2004). The nomenclature of Harty et al. (1997) was used when assigning map units. Colored dots represent averaged offset values measured for alluvial fan remnants of af1 (referred to as Af1 in DuRoss (2004) (blue dots), af2 and afb (referred to as Af2y and Af2o, respectively, in DuRoss (2004) (red dots), and afo (referred to as Af3 in DuRoss (2004) (green dots)). All data points have a one standard deviation error bar. Offset measurements for af1 and af2 correspond well with previous offset measurements while afo only corresponds well near Red Canyon. Results for afo from SOA just north of Willow Creek and North Creek were unreliable.
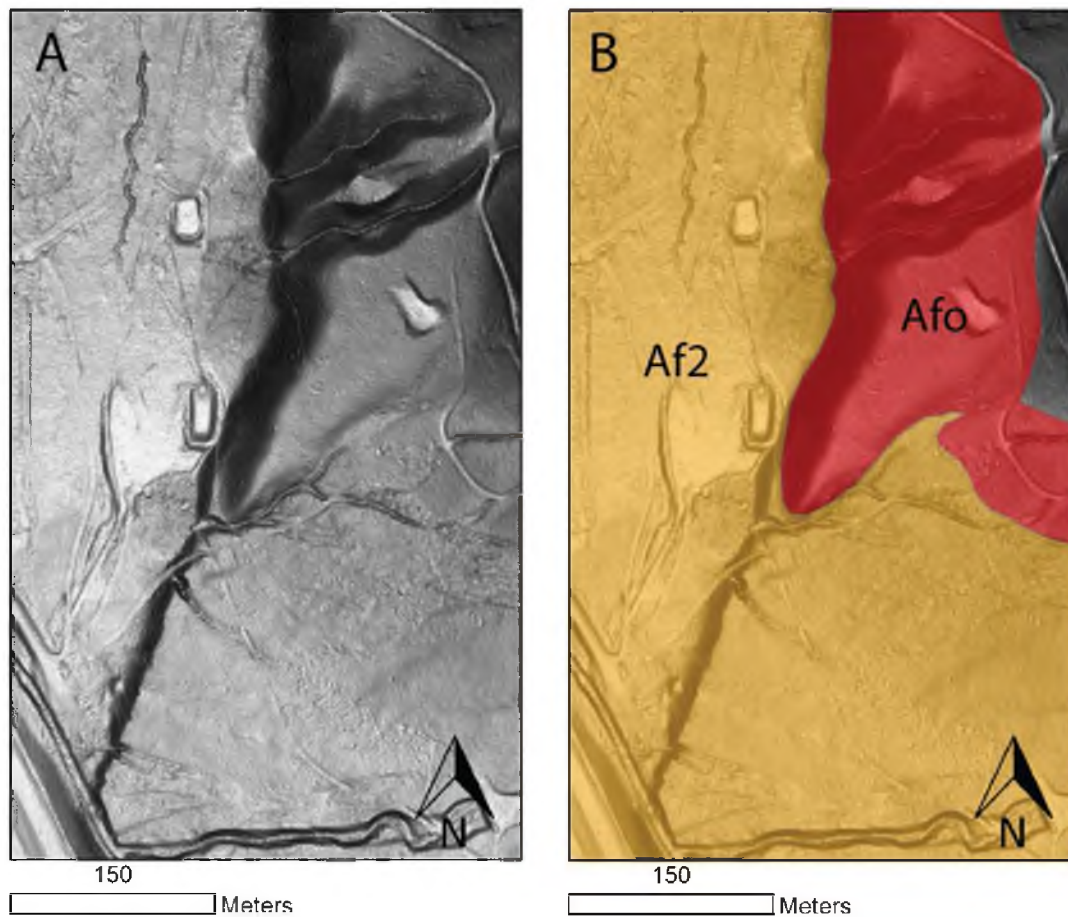
Figure 24: Slopeshade map (A) and slopeshade map overlain by mapped alluvial fan units (B). The LiDAR-derived slopeshade map illustrates the surface roughness contrast between alluvial fan units Af2 (orange) and Afo (red). Afo is a smoother surface with more rounded topographic features, such as scarp crests, than Af2.
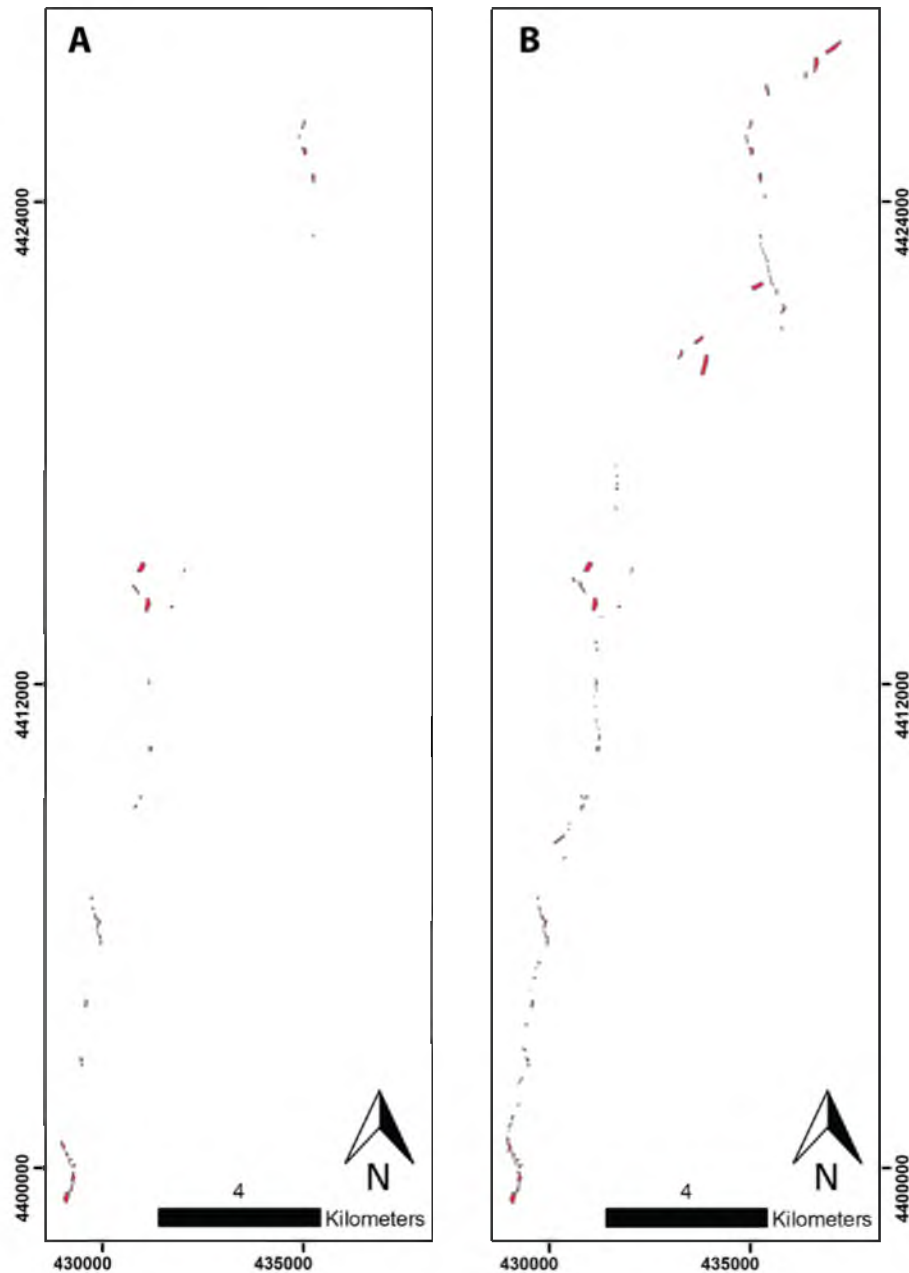
Figure 25: Maps illustrating A) only alluvial fan remnants on the footwall of the Nephi segment within the LiDAR survey area that are able to be assigned a relative age from previous mapping (Harty et al., 1997) or LiDAR mapping (35 remnants in total), and B) all alluvial fan remnants on the footwall of the Nephi segment within the LiDAR survey area that are identifiable on the LiDAR-derived hillshade maps (120 remnants in total). There are at least 85 alluvial fan remnants that lack relative age data within the survey area. The spatial distribution and coverage of relative age data could be greatly improved by more detailed surficial geologic mapping and study of soil development.
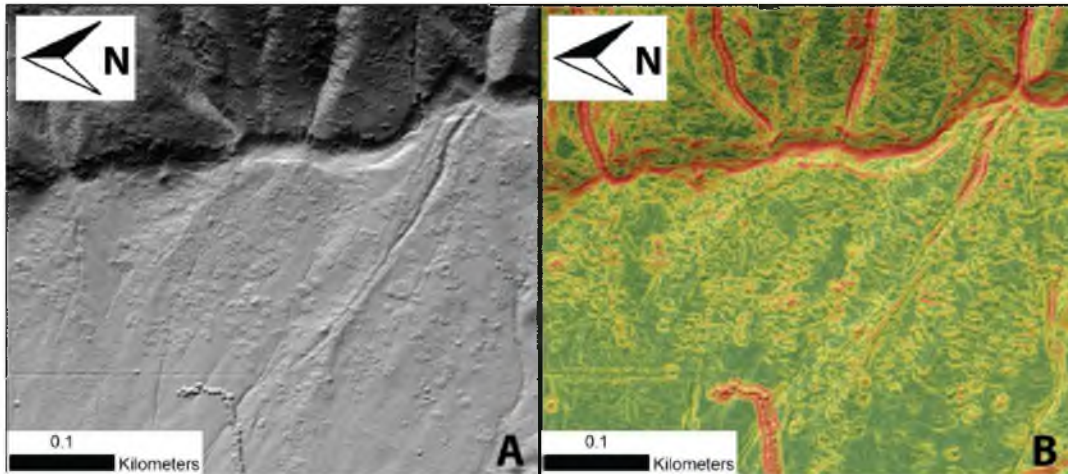
Figure 26: LiDAR-derived hillshade map (A) and roughness map (B) (green-yellow-red color scale indicating smooth-semirough-rough), calculated as the standard deviation of slope, illustrating the effects of poorly filtered vegetation near the fault on roughness calculations. The unusual topography caused by the poorly filtered vegetation cause roughness maps to be unhelpful in differentiating relative ages of alluvial fan remnants.

Table 3: Comparison of Field Surveyed Surface Offset Results with SOA Surface Offset Results

Profile	Field Survey (m)	SOA Result (m)	Difference (%)
Jackson (1991)	1.4	2.3	64
Mattson & Bruhn (2001)	6.0	6.5	8.3
Mattson & Bruhn (2001)	20.0	19.9	0.5
Harty et al. (1997)	3.9	4.2	7.7
DuRoss (2004) Prof. 16	1.6	2.1	31
DuRoss (2004) Prof. 17	7.4	6.5	12
DuRoss (2004) Prof. 1	5.2	3.9	25
DuRoss (2004) Prof. 2	6.4	6.6	3.1
DuRoss (2004) Prof. 7	7.0	6.1	13
DuRoss (2004) Prof. 8	6.4	6.4	1.6
DuRoss (2004) Prof. 9	8.5	9.6	13
DuRoss (2004) Prof. 11	7.5	6.9	8.0
DuRoss (2004) Prof. 52	2.4	1.8	25
DuRoss (2004) Prof. 24	3.4	2.8	18
DuRoss (2004) Prof. 46	1.0	1.8	80
DuRoss (2004) Prof. 56	4.4	4.1	6.8
DuRoss (2004) Prof. 59	1.2	1.6	33
Mean Difference (%)			21

CHAPTER 6

PROTOTYPE PROBABILITY ANALYSIS OF SCARP OFFSET

The 3D-PDF is a hybrid probability density function (PDF) that is useful for

statistical analysis of fault scarp offset and also provides basic information, such as along

strike displacement trends, for geodynamic modeling of fault rupture. The 3D-PDF

expresses the frequency of displacement magnitudes within a specified sampling window

or 'length' of the scarp trace. The sampling window is then moved laterally a specified

amount and the frequency of displacements again calculated using the displacement

observations in the window. The PDF is expressed in a 3D plot in which horizontal x-axis

is length along the fault, the y-axis is displacement magnitude, and the z-axis is frequency

of occurrence of the magnitude of scarp offset within each sampling window. The

resulting plot shows how the distribution of scarp offset changes along the fault and

partially filters out spatial fluctuations in scarp offset related to errors in assignment of

surface deposit age and natural variability in fault slip along strike (e.g., Gudmundsson,

2003; Sagy et al., 2007). The plot is especially useful for evaluating generalized patterns

of fault rupturing and offset along strike, which arise because of the mechanical

properties of the earth's crust, stress concentrations near the ends of faults strands, and

between overlapping fault strands (Cowie and Scholz, 1992; Watterson, 1986; Walsh and

Watterson, 1988; Crider and Pollard, 1998). Constraining the probability of fault offset

magnitude where constructed features (e.g., pipelines and bridges) cross an active fault is

also a potential application of the 3D-PDF.

The 3D-PDF is used in this thesis to carry out a preliminary test of fault rupturing scenarios, including rupture segmentation along the Nephi fault segment. The results are not considered robust because further work is needed to refine the ages of offset alluvial fans and other deposits along the length of the segment. The goal is, instead, to show how such a statistical function is created and plotted, and how it may be useful in the future for carrying out robust analysis of fault rupture modeling. The potential for site-specific probability estimates of fault offset is not discussed further, but the potential for that application remains. The parameters for the rupture models were chosen to represent several rupture scenarios including full fault rupture with a continuous displacement profile along strike, coeval fault rupture with separate displacement profiles for the northern and southern segments, segmented fault rupture, and partial fault rupture. Each model is compared with the 3D-PDFs produced from the empirical offset data to evaluate potential rupture scenarios.

Methods

Introduction to 3D-PDF Calculations and Graphing

The 3D-PDFs are displayed as a frequency distribution plot of offset data within a 1,000 m sample window along the length of the fault, and a surface offset bin size of 0.5 m. The frequency distribution plots are normalized so that the area under each curve is equal to one. The resulting PDF is represented graphically with offset values plotted along the x-axis and the probability of specified displacements on the y-axis (Figure 27). The results are plotted in y-z space at the center of each sampling window along the x-axis. This process is repeated along the length of the fault by continuously stepping along

the fault in 100 m increments and producing PDFs using the 1,000 m sample window (variations in the sample window and length are discussed below). The sampling starts with the trailing edge of the sample window at the southernmost offset measurement and ends when the trailing edge of the sample window reaches the northernmost offset measurement. Because of the north-south trend of the majority of the fault scarps, the sampling window and step direction were fixed with a north-south orientation (Figure 28). By rotating the plot so that the x-axis is horizontal, y-axis is vertical, and assigning a colormap to the z-values, the offset probabilities along the length of the fault are displayed in map view (Figure 29).

A data-sampling window of 1,000 m, a 100 m window offset, and a surface offset bin size of 0.5 m produced the most optimal 3D-PDF results for visual analysis (Figure 30, 31). The 1,000 m window is small enough to reveal detail but not so small that trends are obscured by abrupt fluctuations in offset. The bin size of 0.5 m provides the highest resolution without introducing significant noise to the image. Larger bin sizes (e.g., 1 m or greater) do not provide sufficient resolution for interpreting fault offset trends. The step size of 100 m was chosen to provide significant overlap of data and to produce a dense mesh for creating the probability map. Variations of window, step, and bin size between 250 and 2,000 m, 50 and 1,000 m, and 0.3 and 1.0 m, respectively, did not strongly influence large-scale trends nor overall patterns of offset probability, but did affect the amount of smoothing of the probability function or plot (Figure 30).

A fault trace map aligned above the 3D-PDF (Figure 29) is helpful for identifying the location and size of data gaps where there are no measurements of offset along the fault trace. If a data gap is shorter than the sampling window, it is completely obscured in

the 3D-PDF plot. If the gap is longer than the sampling window, the gap is partially

obscured. PDF slices, produced where a portion of the sampling window is in the gap,

represent a smaller sampling of offset data than typical PDF slices where no data gap was

sampled.

Observations

3D-PDF of Fault Surface Offset without Filtering by Surface Age

I produced a 3D-PDF of the Nephi segment offset data using the 1000-m

sampling window and 0.5-m bin-size parameters described above (Figure 29). Peaks in

surface offset range from 0.5 to 12 m. The most prevalent peaks in offset are at 2, 4, and

6 m with less prevalent peaks at 8-12 m. The northern and southern strands of the

segment each have a pattern of displacements tapering toward the ends of the strands.

The southern strand has higher overall offset values (maximum peak values of 10-12 m)

while the northern strand has lower overall offset values (maximum 6-8 m). The northern

segment exhibits two large, broad peaks of ~2-4 m surface offset at 20 km and 30 km

along strike. These raise questions of how to interpret the shapes and patterns observed in

a 3D-PDF of surface offset. In order to answer these questions, the factors that influence

the 3D-PDF must be identified.

Effects of Surface Deposit Age and Fault Orientation on the 3D-PDF

Overlaying a map of the fault showing ages of alluvial fans over the 3D-PDF

allows along strike offset trends to be correlated with the geomorphology and ages of

deposits. The age, preservation, and spatial distribution of the alluvial fan units have a

large influence on the shape of the 3D-PDF. The best preserved and most prevalent

alluvial fan unit along the southern strand of the Nephi segment is unit af2. This fan unit

has an average surface offset of ~6 m and peaks in offset near 6 m are prevalent throughout the southern strand (e.g., at 2, 10, and 18 km; Figure 29). Peaks in offset near 2-3 m along the southern fault strand are probably related to the younger af1 unit, which has an average surface offset of ~3 m. On the northern strand there is a lack of ~6 m peaks. This could suggest poor preservation of af2 or less displacement on af2 surfaces. Unfortunately, interpreting the 3D-PDF is complicated by the poor age control for many of the offset geomorphic surfaces: 76 percent of the offset data produced by SOA could not be assigned age data. Therefore, the unassigned data have the largest contribution to the 3D-PDF and introduce uncertainty in making interpretations from the patterns observed in the 3D-PDF.

An area of the fault oriented obliquely to the sampling window may bias the 3D-PDF. This oblique orientation causes the offset data density (offset data points per meter along sampling window) for that portion of the fault to be anomalously high. This has two contrasting effects on that portion of offset data's contribution to the 3D-PDF. Portions of obliquely oriented fault more heavily influence singular PDF slices that sample the obliquely oriented fault. However, that section of fault will also be sampled in fewer PDF slices due to its orientation to the sampling window, minimizing its lateral influence on the 3D-PDF's shape. The only large sections of obliquely oriented fault scarps are located at the north end of the northern strand and in the fault step-over between the two strands (~20 km along strike). At both of these locations, the probabilities collapse to high, narrow peaks due to the increased influence of these oblique fault sections on PDF slices (Figure 29). Stepping parallel to the fault trace at all time would eliminate this data density variation.

SOA treats multiple fault traces separately and does not collocate their offsets. This can cause peaks in offset to be lower than they actually are. If two parallel scarps have ~2 m of offset the 3D-PDF will show a peak at 2 m instead of the appropriate 4 m peak. This issue can be fixed by collocating offset values for multiple parallel scarps instead of treating them separately.

Fault Displacement Models

<u>Background: Fault Displacements</u>

An important question is whether the 3D-PDF can help resolve the along strike patterns of surface rupture on an individual fault or segment. Several models of faulting have been proposed to predict the distribution of displacement along the length of a fault, both as the result of seismic slip during an earthquake, and cumulative slip acquired over multiple earthquake or sliding events. Cowie and Scholz (1992) use a fracture mechanics model with a 'plastic' crack zone surrounding the fault tips. Fault displacement is maximized at the center of the fault and tapers towards zero at the tips (Figure 32a). Near the fault tips, displacement exhibits a concave-up trend due to increased shear stress caused by frictional resistance to sliding within the fractured tip zone.

Watterson (1986) and Walsh and Watterson (1988) model along strike fault displacement by an elliptical distribution of fault slip, which may be theoretically justified, based on simple linear elastic fracture mechanics modeling where no 'plastic' deformation zone surrounds the fault tip (Watterson, 1986; Walsh and Watterson, 1988). The half-ellipse displacement pattern also has maximum displacement at the center of the fault and displacement decreases to zero at the tips. However, in this model, unlike that proposed by Cowie and Scholz (1992), the displacement pattern is concave-downwards

towards the tips of the fault (Figure 32b). The half-ellipse has been cited as a valid model for along strike fault displacement for Basin and Range normal faults based on empirical data (Olig, 1994; Pezzopane and Dawson, 1996), and has also been utilized to model displacement along the Wasatch fault and the San Andreas fault (Chang and Smith, 2002; DuRoss, 2008; Biasi and Weldon, 2006; Biasi and Weldon, 2009).

Crider and Pollard (1998) produced numerical models of overlapping fault strands or fault step over zones. Their modeling suggested that the largest offsets are grouped near the overlapping ends of the fault strands, rather than in the central part of each strand (Figure 32c). This model may apply to the Nephi fault segment, where the northern and southern strands of the segment overlap on each other, and also where the northern strand of the Nephi segment overlaps with the Provo segment for a lateral distance of ~15 km (Figure 1).

Model Parameters

All displacement models were calculated by simulating surface-faulting earthquakes or 'events' on the Nephi segment. The three youngest events were modeled because most paleoseismic trenching investigations have found evidence for three surface-rupture events on scarps offsetting af2 alluvial fans (mid-Holocene) (Hanson et al., 1981; Jackson, 1991; Machette et al., 2007). There are also a significant number of afb alluvial fan remnants (uppermost Pleistocene), which in general have greater offsets than the af2 alluvial fans. Therefore, the fourth event was added to account for the presence of older afb fans with greater offsets than the af2 fans.

Model A assumes that the northern and southern strand of the Nephi segment rupture as one continuous fault with no tapering off of displacement between the southern

and northern fault sections (Figure 33A). The earthquake events are modeled to produce a

continuous surface rupture along the entire length of the fault with an average surface

offset of ~2 m. This value was chosen as an average of surface offset values produced

from fault trenching studies along the Nephi segment. The offset is modeled by the

following equation where s(i) is surface offset, x(i) is along strike distance, and l is the

total length of the fault segment.

$$s(i) = 2.67 \sin\left(\frac{x(i)\pi}{l}\right)^{0.5} \tag{3}$$

In Model B, the northern and southern strands rupture coseismically in Nephi

segment earthquakes, but have separate displacement profiles (displacement decreasing

to zero at the step over) (Figure 33B). This creates distinct displacement curves along

each strand, modeled using equation (3). Although modeling of slip patterns across

normal fault step over zones by Crider and Pollard (1998) predicts distinct displacement

curves for each strand that both are skewed toward the step over, I only used symmetric

displacement curves to maintain simplicity in modeling.

Model C assumes the same fault behavior as Model B except that the northern

strand has a lower average offset of ~1.5 m per event based on the scaling of fault

displacement with surface rupture length (Wells and Coppersmith, 1994) (Figure 33C).

The offset for the northern strand is modeled by the following equation:

$$s(i) = 2.0 \sin\left(\frac{x(i)\pi}{l}\right)^{0.5} \tag{4}$$

In Model D the fault is modeled with segmented behavior and with average

offsets per event of ~2 m for the southern strand. The northern strand is modeled with an

average offset per event of ~3 m based on trenching data from DuRoss (2008). This

model assumes that the southern strand has four surface-rupture events while the northern strand only experiences two surface-rupture events (Figure 33D).

The offset for Model E is modeled by the same equation as in Model A, however, the southern strand ruptured during the most recent event and the third event. The entire fault is ruptured during the second and fourth events (Figure 33E).

Modeling Results

The displacement models were overlain on the full data 3D-PDF of the Nephi segment to compare the along strike displacement pattern (Figure 34). Model D, and to a lesser extent Model B, provide the closest matches to the observed along strike displacement patterns for the Nephi segment. Model E provides a fair match to the observed along strike displacement patterns for the Nephi segment, but does not fit as well as D or B. Models A and C do not fit the fault segment's observed displacement PDF and are considered not viable.

Model D closely follows the trends in along strike displacement for the Nephi segment data. This model is the best fit for the northern strand with the two events with an average offset of ~3 m. Model B also is a very good fit for the northern strand with four events with a smaller average offset of ~2 m. While both models are a good fit for the northern strand, Model D's parameters are supported by paleoseismic data from DuRoss (2008) making it a better overall fit. Model E matches the slight tapering of offset values where the northern and southern strand approach each other but it fails to encompass some higher offset values in the northern strand around ~25 km along strike.

Model C is a poor fit for the northern strand offset pattern. Unlike models B and D, it does not fit the large offset observed on the fault strand (Figure 33). Model A

encompasses the higher offsets in the northern strand but fails to encompass the highest offsets in the southern strand from 0-15 km along strike making it a poor fit for the Nephi segment data as well.

Interpretation of Fault Displacement Modeling

The earthquake scenario models suggest separate displacement profiles for the northern and southern strands of the Nephi segment. Although some models are based on segmented behavior of the two strands (e.g., Model D, the best fitting model), conclusions on segmented behavior cannot be made from these models. Regardless of segmented behavior, the northern strand presumably does not rupture independently because the magnitude of offsets (3 m) observed along the northern strand suggests a surface rupture length of at least 50 m (DuRoss et al., 2008). An avenue for further investigation is whether the northern strand of the Nephi segment ruptures with the southern strand, the Provo segment, or a combination. Further progress is inhibited by the lack of data on the age of surface deposits along the length of the fault.
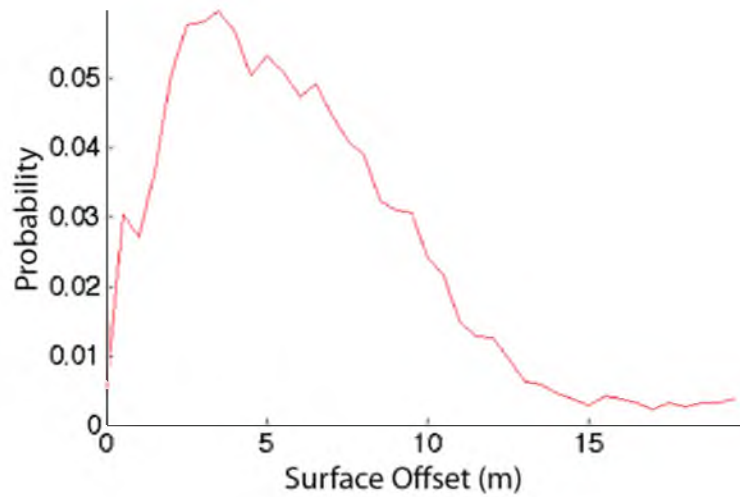
Figure 27: A single probability density function (PDF) plot produced by making a normalized frequency plot of surface offset data sampled in a 1000 m window along the fault with a bin size of 0.5 m. Peaks in the plot represent the most common offset measurements found in the dataset.

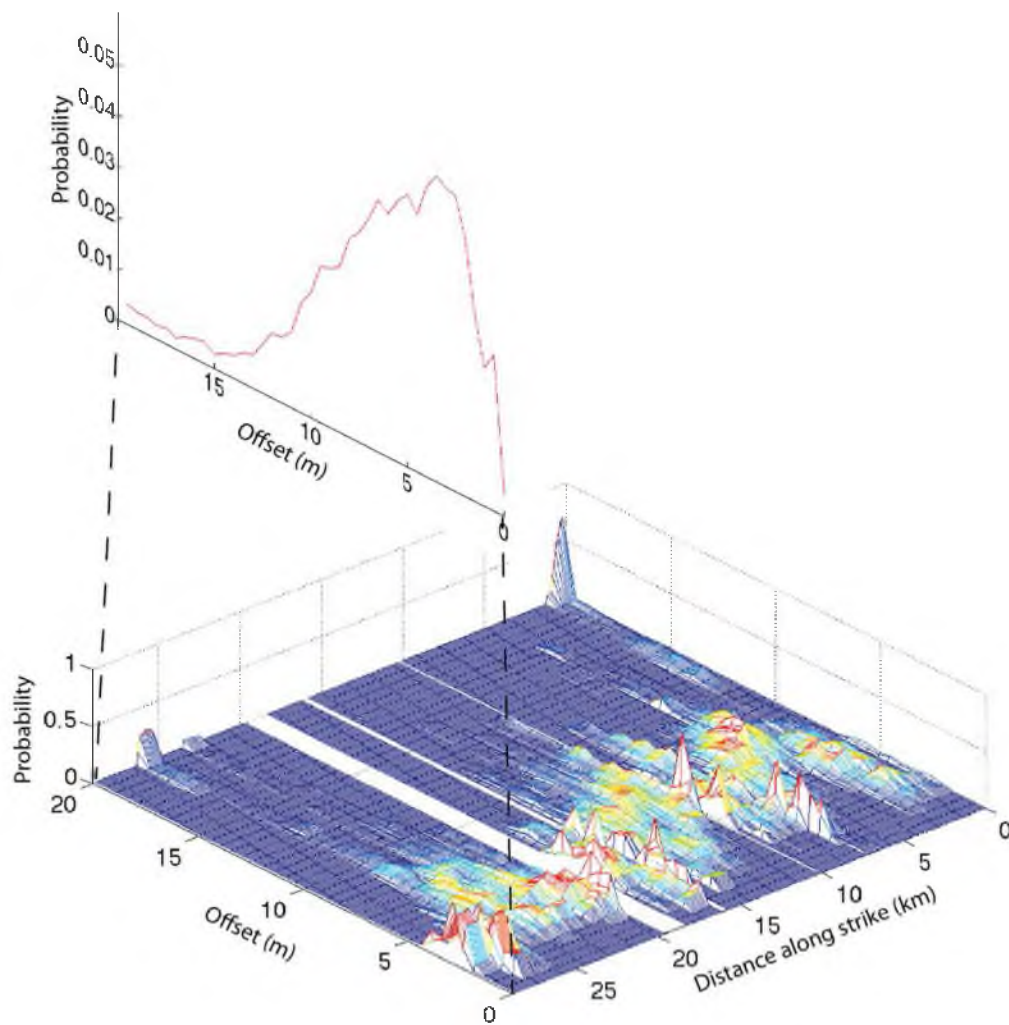Figure 28: Individual PDFs are calculated along strike of the fault using a 1,000 m sample window of offset data (0.5-m bin size). The window is moved 100 m along strike and then the PDF is calculated again. These PDFs are aligned to produce a 3D-PDF plot of offset along the length of the fault (lower plot showing distance, offset, and probability). This plot is a 3D representation of along strike trends in scarp offset.
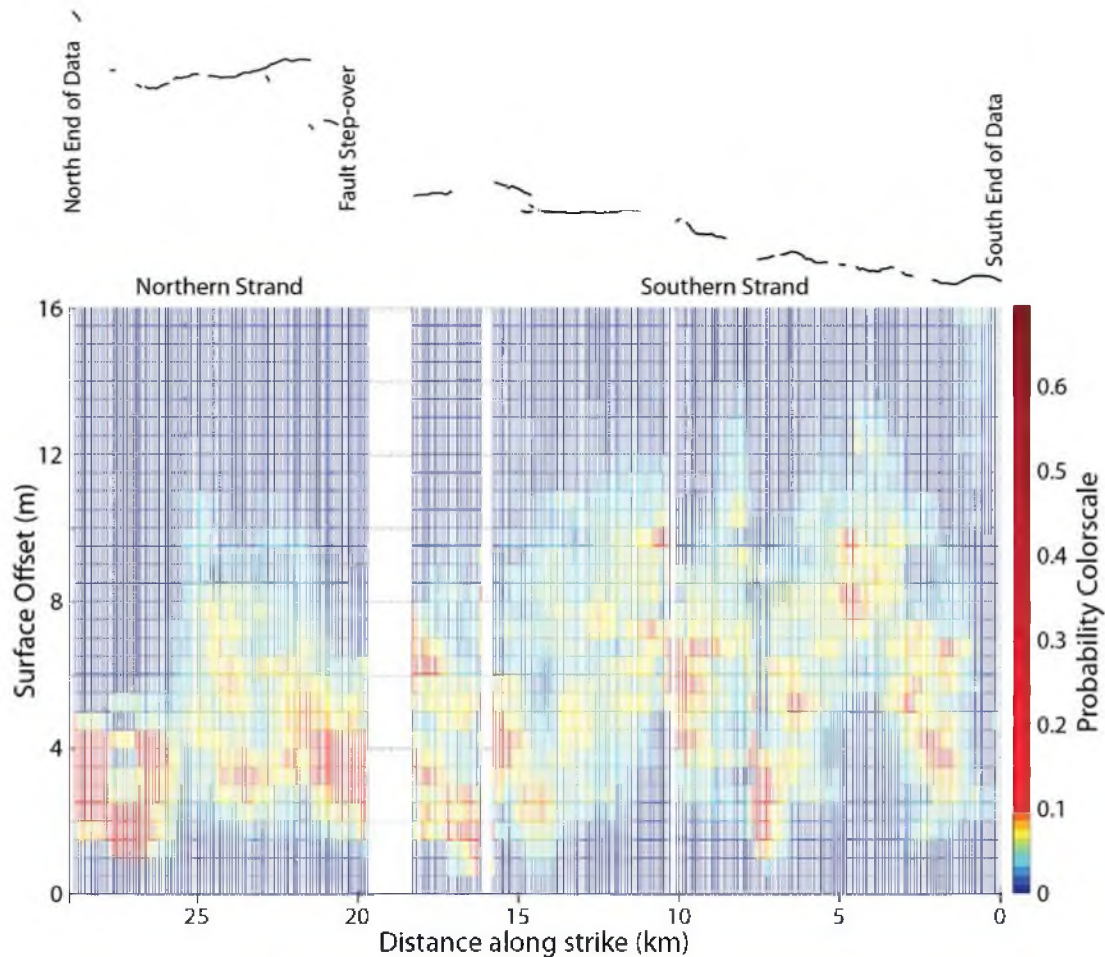
Figure 29: 3D-PDF plot of surface offset probability along the Nephi segment of the Wasatch fault. At a point along the fault, the 3D-PDF shows the normalized probability of displacement (in a 1000 m sample window) corresponding with the color scale at right. This plot shows only the section of the Nephi segment with LiDAR data coverage, not the entire length of the fault. The southern strand exhibits strong peaks in displacement at 6-8 m. The southern strand also exhibits peaks at 2-4 m, and 10-12 m. The northern strand has its strongest peaks at 2-4 m and exhibits overall lower offsets along the entire strand than the southern strand. It is likely that the two strands, which are separated by a fault step-over boundary, have unique along strike displacement profiles.
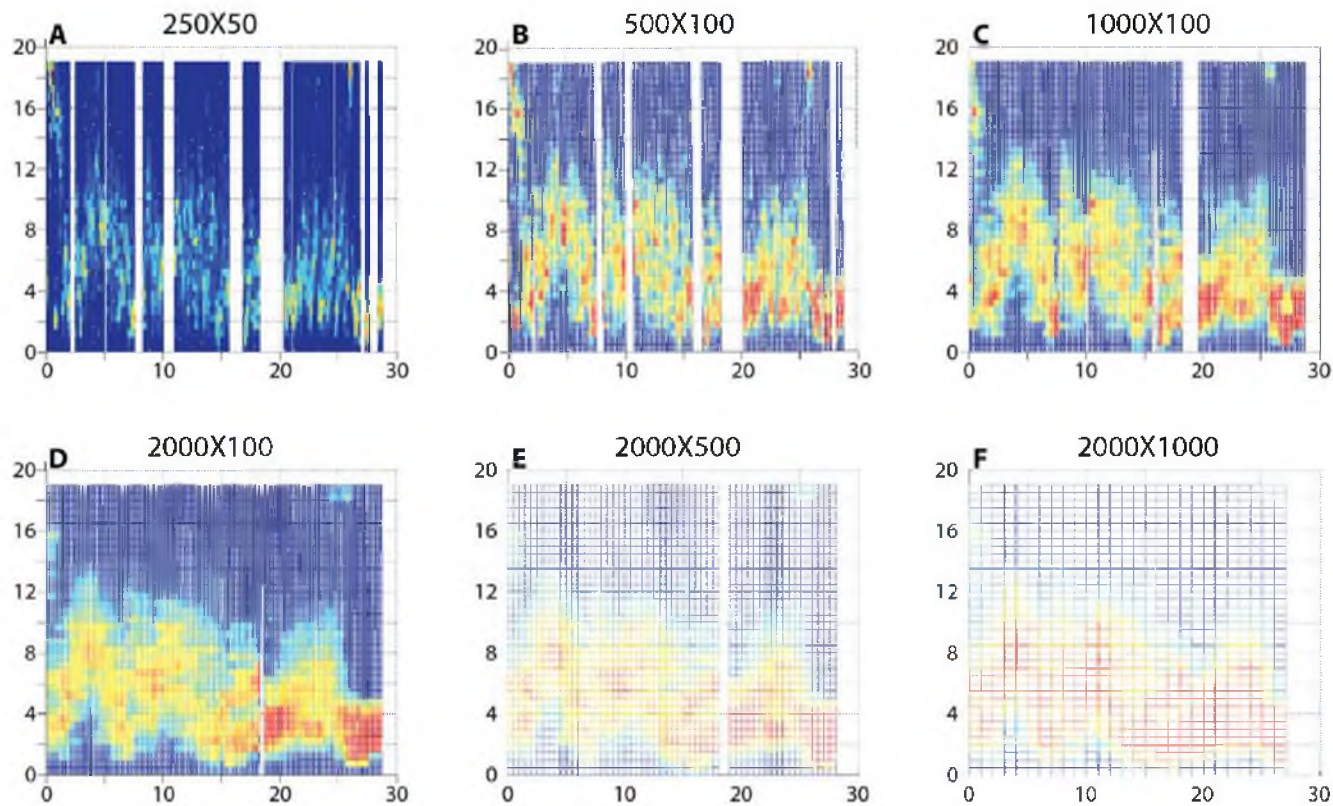
Figure 30: 3D-PDF plots produced with various window and step sizes. Plot titles are in the format (window size)X(step size), both in meters: A) 250 X 50, B) 500 X 100, C) 1,000 X 100, D) 2,000 X 100, E) 2,000 X 500, F) 2,000 X 1,000. The y-axis is surface offset, the x-axis is distance along fault strike with zero starting at the southern end of the fault, and the z-axis is oriented perpendicular to the page and represents probability. The color scale represents low probability as cool colors and high probability as warm colors. The window and step size of 1,000 X 100 shows the optimal amount of surface-offset detail while minimizing noise caused by small-scale variations in offset along strike.
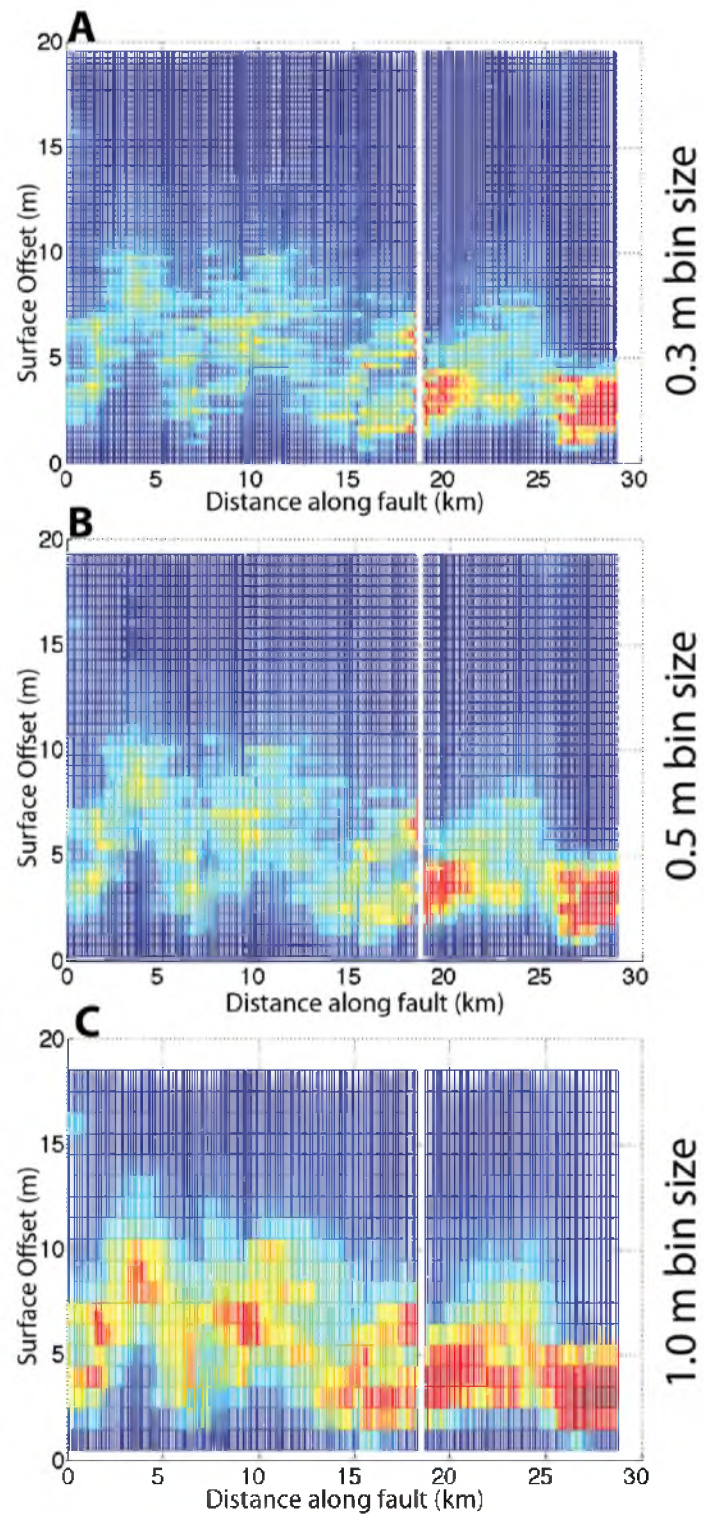
Figure 31: 3D-PDF plots showing the effect of varying surface offset bin size. A) 0.3 m bin size, B) 0.5 m bin size, and C) 1.0 m bin size. The 0.5 m bin size preserves detail without introducing too much noise to the image.
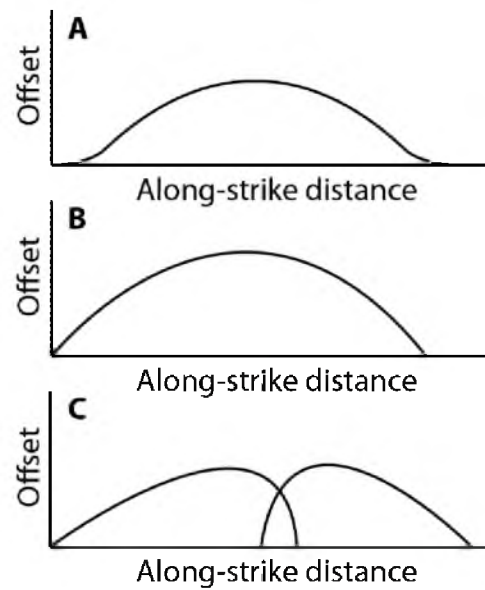
Figure 32: Theoretical models of along strike displacement. A) Plastic tip-zone model (Cowie and Scholz, 1992); B) half-ellipse: simple linear elastic fracture mechanics model (Watterson, 1986; Walsh and Watterson, 1988); C) fault step-over zone overlap model (Crider and Pollard, 1998).
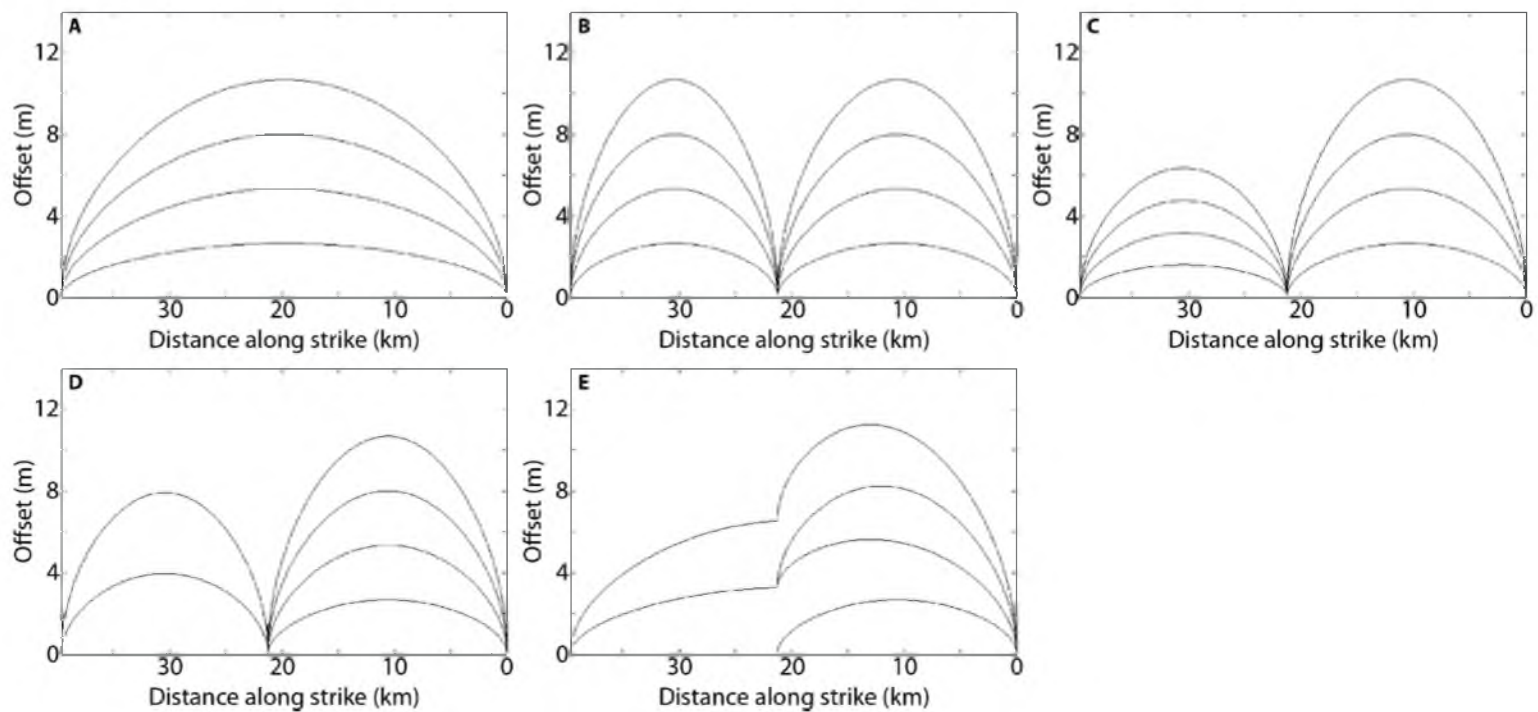
Figure 33: Synthetic models of displacement profiles. A) Simple full-length ruptures with curved displacement profile. B) Coseismic rupture behavior with separate curved displacement profiles. C) Coseismic rupture behavior (the strands rupture together) with separate curved displacement profiles. The northern strand experiences less displacement per event. D) Segmented rupture behavior (the strands rupture independently of each other) with curved displacement profiles. The northern strand experiences only two surface rupture events while the southern strand experiences four. E) Rupture model where the last most recent and third event rupture only the southern strand while the second and fourth event rupture the whole segment.
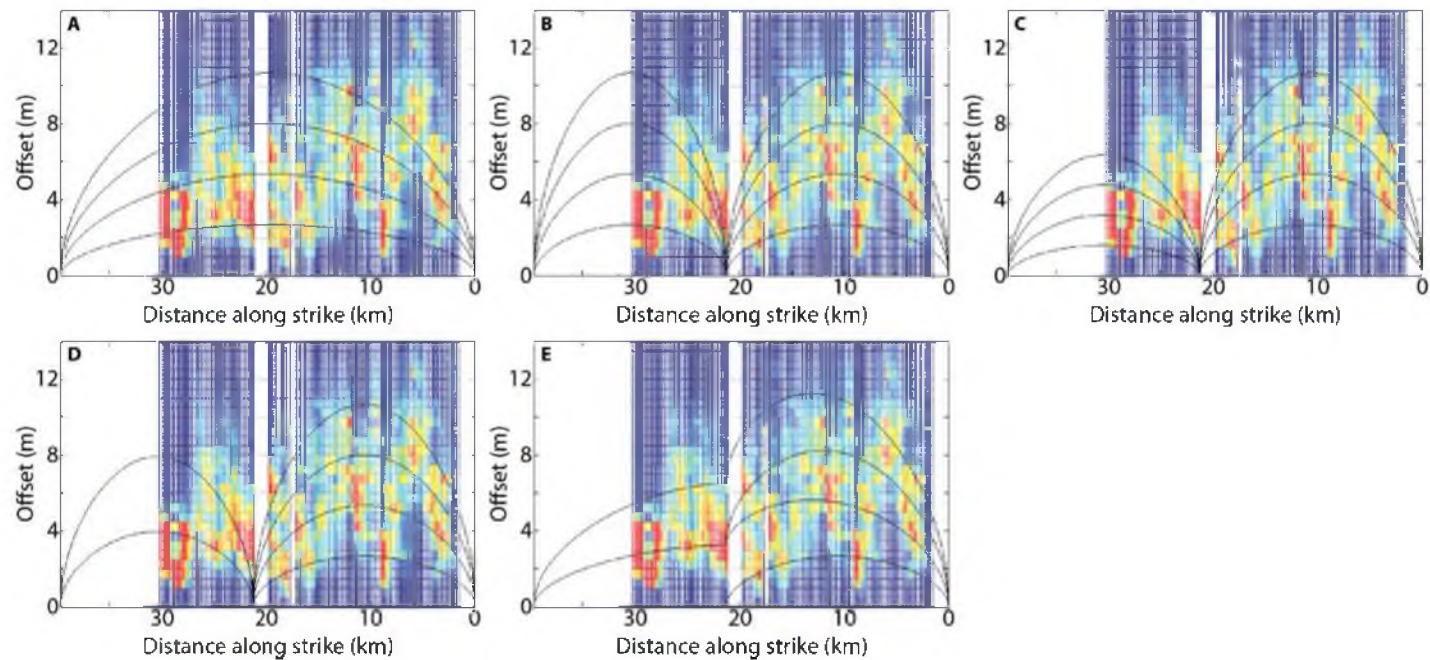
Figure 34: Synthetic models overlain on the 3D-PDF of the Nephi segment from Figure 29. A) Simple full-length ruptures with curved displacement profile. B) Coseismic rupture behavior with separate curved displacement profiles. C) Coseismic rupture behavior (the strands rupture together) with separate curved displacement profiles. The northern strand experiences less displacement per event. D) Segmented rupture behavior (the strands rupture independently of each other) with curved displacement profiles. The northern strand experiences only two surface-rupture events while the southern strand experiences four. E) Rupture model where the last most recent and third event rupture only the southern strand while the second and fourth event rupture the whole segment. Visual comparison of each model's fit to the Nephi segment offset data can be made. Models A and C match least well while Model D best matches the along strike displacement profile of the Nephi segment. This would suggest separate displacement profiles for the northern and southern strands of the Nephi segment with the northern strand having a higher average offset per event. More detailed discussion of the models and their implications are found in the text.

CHAPTER 7

CONCLUSIONS

SOA, scripts that allow for the semi-automated generation of topographic profiles

and measurement of scarp offset, extends the ability of commercial GIS software to

analyze normal fault scarps. SOA software rapidly generates scarp topographic profiles

and offset measurements utilizing very high-resolution elevation models created by

LiDAR surveying. The software is written in the Python scripting language and is

compatible with common proprietary and open source computer operating systems.

The software algorithms were tested and verified utilizing 0.5 m posted bare earth DEMs

acquired by the National Center for Airborne Laser Mapping using airborne Light Detection

and Ranging (LiDAR) along the Nephi segment of the Wasatch normal fault. The

topographic profiles and scarp offsets generated by SOA were compared with selected

profiles and offset measurements determined by surveying on the ground. The mean

difference in scarp offset determined by the two techniques was 21 percent when averaged

at 17 ground-surveyed locations across the fault.

One limitation of the SOA algorithms is the inability to analyze complex fault

scarps. This includes multiple surface breaks within a scarp embankment and areas where

antithetic scarps dip back towards the primary fault scarp. These limitations may be

removed with further development of the algorithms.

SOA software was used to measure scarp offset at 36,757 locations along the

Nephi segment, with separation between most localities of ~ 1 m. After visual inspection for complications in fault scarp morphology and errors in picking scarp crests and bases, 19,798 profiles and offset measurements were deemed suitable for further analysis. Analysis of the resulting scarp data shows a marked variation in offset along strike that is related to several features including a) ages of surface deposits, b) natural variation in fault offset along strike, and c) the presence of fault step-overs. The lack of high-resolution geological mapping and incomplete knowledge of ages of faulted surface deposits are significant factors that limit the ability to refine the history of faulting along the Nephi segment using SOA.

The SOA results reveal significant natural variability in surface offset and illustrate the limitations of selecting a single scarp profile to quantify offset over distances as small as tens of meters along strike. The ability to measure and quantify this natural variability in offset is a significant advancement in technique provided by the high-resolution LiDAR dataset and SOA software. A 3D probability density plot of surface offset along strike was therefore developed to aid interpretation of the offset data. The 3D-PDF was used to carry out a preliminary test of fault rupturing scenarios, including rupture segmentation along the Nephi fault segment. Results suggest that the northern and southern strands of the Nephi segment each have unique displacement profiles, which is important for modeling along strike trends in surface-faulting earthquake rupture.

APPENDIX

SOFTWARE PROGRAMS

line_maker.py

```python
import numpy as np
from numpy import *

#Enter the path and filename for the file created in Step 5 of Section 4.5
f = 'path/filename.txt'
# Loads the data into two single column arrays of ref, x, and y data
zero, null, x, y = loadtxt(f, delimiter = ',', skiprows=1, unpack=True)

#create a place to store x_start, y_start, x_end, and y_end
x_start = []
y_start = []
x_end = []
y_end = []

#define the amount of offset in m
offset = 100

#calculate the slope of perpendicular line to point
for i in range(0, len(x)-1):
        if i == 0:
                m = -(x[i+1] - x[i]) / (y[i+1] - y[i])
        elif i == (len(x)-1):
        m = -(x[i] - x[i-1]) / (y[i] - y[i-1])
        else:
                m = -(x[i+1] - x[i-1]) / (y[i+1] - y[i-1])
        x_s = x[i] - cos(arctan(m)) * offset
        y_s = y[i] - sin(arctan(m)) * offset
        x_e = x[i] + cos(arctan(m)) * offset
        y_e = y[i] + sin(arctan(m)) * offset
        x_start.append(x_s)
        y_start.append(y_s)
        x_end.append(x_e)
        y_end.append(y_e)
```

```
#Specify a file path and name for import to GIS application in Step 7 of Section 4.5
f1 = 'path/filename.txt'
target = open(f1, 'w')

target.write('x_start,y_start,x_end,y_end,x,y')
target.write('\n')

for i in range(0, len(x)-1):
    b = str(x_start[i])
    c = str(y_start[i])
    d = str(x_end[i])
    e = str(y_end[i])
    g = str(x[i])
    h = str(y[i])
    target.write(b)
    target.write(',')
    target.write(c)
    target.write(',')
    target.write(d)
    target.write(',')
    target.write(e)
    target.write(',')
    target.write(g)
    target.write(',')
    target.write(h)
    target.write('\n')

target.close()
```

separator.py

```
import numpy as np
from numpy import*

#Input the path and filename created in Step 10 of Section 4.5
file = 'path/filename.txt'

#Open the file
FID_1, ORIG_FID, POINT_X, POINT_Y, Z, cr, ff = loadtxt(file, delimiter = ',',
unpack=True)

#Define the number of profiles contained in the file.
l = int(ORIG_FID[len(ORIG_FID)-1])
```

```python
#For every profile create a seperate file for the profile.
for i in range(0, len(ORIG_FID)):
        if i == 0:
                a = str(int(ORIG_FID[i]))
#Define path and filename to store the seperated xy profiles
                filename = 'path/filename/%s.txt' % a
                f = open(filename, 'w')
                x = str(POINT_X[i])
                y = str(POINT_Y[i])
                z = str(Z[i])
                s = str(ff[i])
                d = str(cr[i])
                f.write(x)
                f.write(',')
                f.write(y)
                f.write(',')
                f.write(z)
                f.write(',')
                f.write(s)
                f.write(',')
                f.write(d)
                f.write('\n')
        elif ORIG_FID[i] == ORIG_FID[i-1]:
                x = str(POINT_X[i])
                y = str(POINT_Y[i])
                z = str(Z[i])
                s = str(ff[i])
                d = str(cr[i])
                f.write(x)
                f.write(',')
                f.write(y)
                f.write(',')
                f.write(z)
                f.write(',')
                f.write(s)
                f.write(',')
                f.write(d)
                f.write('\n')
        else:
                f.close()
                a = str(int(ORIG_FID[i]))
#Enter same path and filename as on line 18 above
                filename = 'pathe/filename/%s.txt' % a
                f = open(filename, 'w')
                x = str(POINT_X[i])
                y = str(POINT_Y[i])
```

```python
        z = str(Z[i])
        s = str(ff[i])
        d = str(cr[i])
        f.write(x)
        f.write(',')
        f.write(y)
        f.write(',')
        f.write(z)
        f.write(',')
        f.write(s)
        f.write(',')
        f.write(d)
        f.write('\n')
f.close()



#Create a seperate file for a normalized profile
#Each profile contains x, y, and z information
#this combines the x and y into a single horizontal distance
#which makes a 2d profile
for i in range (0, l+1):
    a = i
#Enter same path and filename as on line 18 above
    filename =
'/uufs/cmes.utah.edu/data/u0322532/nephi/full/north_reg/xy_profiles/%s.txt' % a
#Enter new path and filename to store 2d profiles
    prof_filename = 'path/filename/%s.txt' % a
    f = open(prof_filename, 'w')
    X, Y, Z, ff, cr = loadtxt(filename, delimiter = ',', unpack=True)
    distance = []
    for j in range(0, len(X)): #writes the 2d data into a file
        t = sqrt(square(Y[j]-Y[0]) + square(X[j]-X[0]))
        distance.append(t)
        x = str(distance[j])
        y = str(Z[j])
        f.write(x)
        f.write(',')
        f.write(y)
        f.write('\n')
    f.close()
```

soa.py

```python
import numpy as np
from numpy import *
```

```
prompt = '> '

print "Please enter region of analysis:"
region = raw_input(prompt)

#Define path and filename to create file for storing offset and slope data
f = 'path/filename.txt'

#Define path and filename to create file for storing crest data
f1 = 'path/filename.txt'

#Define path and filename to create file for storing base data
f2 = 'path/filename.txt'

target = open(f, 'w')
target.write('ID,max_offset,ff_slope,max_slope,ms_x,ms_y,ms_z,fault_x,fault_y,fault_z')
target.write('\n')
target1 = open(f1, 'w')
target1.write('ID,crest_x,crest_y,crest_z')
target1.write('\n')
target2 = open(f2, 'w')
target2.write('ID,base_x,base_y,base_z')
target2.write('\n')

#Range values should be (zero, number of individual profiles to be analyzed)
#Specify path and filename for filename1: should be filename for storing 2d profile data
created in separator.py
#Specify path and filename for filename2: should be filename for storing xy profile data
created in separator.py
for i in range (0, 27312):
    a = i
    filename1 = 'path/filename/%s.txt' % a
    filename2 = 'path/filename/%s.txt' % a

# Loads the data into two single column arrays of x and y data
    x, y = loadtxt(filename1, delimiter = ',', unpack=True)
    x1, y1, z1, ff, dist = loadtxt(filename2, delimiter = ',', unpack=True)

#define h or change in x
    h = x[1] - x[0]

#create place to store dydx values
    dydx = []

#create place to store dydx2 values
```

```
dydx2 = []

#compute first derivative numerically
    for i in range(0, len(y)-1):
        if i == 0:
            y_prime = (y[i+1] - y[i]) / h
        elif i == len(y):
            y_prime = (y[i] - y[i-1]) / h
        else:
            y_prime = (y[i+1] - y[i-1]) / (2 * h)
        dydx.append(y_prime)

#compute second derivative numerically
    for i in range(0, len(dydx)-1):
        if i == 0:
            dydx_prime = (dydx[i+1] - dydx[i]) / h
        elif i == len(dydx):
            dydx_prime = (dydx[i] - dydx[i-1]) / h
        else:
            dydx_prime = (dydx[i+1] - dydx[i-1]) / (2 * h)
        dydx2.append(dydx_prime)

#Find where the scarp starts.
#Find the maximum of the second derivative within a range close to the base of the scarp

    lower = max(dydx2[180:220])
    base = dydx2.index(lower)

#Find where the scarp ends by finding the min to the mapped crest and then defining a
window around that of +- 5 m
    crest_exists = max(dist)
    if crest_exists == 1:
        mc_index = nonzero(dist == 1)[0][0]
        low = mc_index - 10
        high = mc_index + 10
    else:
        low = 200
        high = 325
#Find the minimum of the second derivative within a range close to the top of the scarp
    try:
        upper = min(dydx2[low:high])
        crest = dydx2.index(upper)
    except ValueError:
        pass

#Find the reference of the base of the scarp
```

```python
base_x = x1[base]
base_y = y1[base]
base_z = z1[base]

#Find the reference of the top of the scarp

crest_x = x1[crest]
crest_y = y1[crest]
crest_z = z1[crest]

# Find the maximum value of dydx
    try:
        m = max(dydx[base:crest])
    except ValueError:
        continue

# Find the index for the max value of dydx
    p = dydx.index(m)

# Find the maximum slope
    import math
    max_slope = math.degrees(math.atan(m))

#Find the numeric x and y data values of the max slope point
    max_slope_horiz = x[p]
    max_slope_vert = y[p]
    max_slope_x = x1[p]
    max_slope_y = y1[p]
    max_slope_z = z1[p]

#Make arrays with lower and upper far-field slope x and y data
    x_low = []
    for i in range(0, base):
        if ff[i] == 2:
            x_copy = x[i]
            x_low.append(x_copy)
        else:
            next

    y_low = []
    for i in range(0, base):
        if ff[i] == 2:
            y_copy = y[i]
            y_low.append(y_copy)
        else:
```

```
        next

    x_high = []
    for i in range(crest, len(x)):
        if ff[i] == 1:
            x_copy = x[i]
            x_high.append(x_copy)
        else:
            next

    y_high = []
    for i in range(crest, len(y)):
        if ff[i] == 1:
            y_copy = y[i]
            y_high.append(y_copy)
        else:
            next

#Compute the best fit line for the upper and lower far-field slopes
    try:
        low_ff = np.polyfit(x_low, y_low, 1)
    except TypeError:
        low_ff = [-0.87266, 0]

    try:
        high_ff = np.polyfit(x_high, y_high, 1)
    except TypeError:
        high_ff = [0.87266, 0]

#Compute slope difference of far-field slopes
    slope_diff = math.degrees(math.atan(high_ff[0] - low_ff[0]))

#Calculate the points to measure offset from the best fit line of the far-field slopes
    offset_top = high_ff[0] * max_slope_horiz + high_ff[1]
    offset_bottom = low_ff[0] * max_slope_horiz + low_ff[1]

#Calculate maximum offset
#If the upper far_field slope is greater than 10 degrees we will measure straight out from the top of scarp
#to the max slope of the scarp and multiply by 2
#If the upper and lower far-field slopes are within 5 degrees we will measure top to bottom
#If the upper and lower far-field slopes aren't within 5 degrees we will measure top to mid and multiply by 2

    if math.degrees(math.atan(high_ff[0])) > 10:
```

```
    try:
        max_offset = (y[crest] - max_slope_vert) * 2
        o = 0
    except IndexError:
        pass
else:
    if slope_diff <= 5.0:
        max_offset = offset_top - offset_bottom
        o = 2
    else:
        max_offset = (offset_top - max_slope_vert) * 2
        o = 1

ID = str(a)
b = str(max_offset)
c = str(o)
d = str(max_slope)
e = str(max_slope_x)
g = str(max_slope_y)
j = str(max_slope_z)
fx = str(x1[200])
fy = str(y1[200])
fz = str(z1[200])
cx = str(crest_x)
cy = str(crest_y)
cz = str(crest_z)
bx = str(base_x)
by = str(base_y)
bz = str(base_z)
target.write(ID)
target.write(',')
target.write(b)
target.write(',')
target.write(c)
target.write(',')
target.write(d)
target.write(',')
target.write(e)
target.write(',')
target.write(g)
target.write(',')
target.write(j)
target.write(',')
target.write(fx)
target.write(',')
target.write(fy)
```

```
        target.write(',')
        target.write(fz)
        target.write('\n')
        target1.write(ID)
        target1.write(',')
        target1.write(cx)
        target1.write(',')
        target1.write(cy)
        target1.write(',')
        target1.write(cz)
        target1.write('\n')
        target2.write(ID)
        target2.write(',')
        target2.write(bx)
        target2.write(',')
        target2.write(by)
        target2.write(',')
        target2.write(bz)
        target2.write('\n')


target.close()
target1.close()
target2.close()
```

stem_plotter.py

```
import numpy as np
from numpy import *

#Enter the path and filename of the file created in Step 5 of Section 4.5
fault_file = 'path/filename.txt'
#Enter the path and filename of the file created using soa.py to store offset and slope data
slope_file = 'path/filename.txt'

# Loads the data
zero, zero, fault_x, fault_y = loadtxt(fault_file, delimiter = ',', skiprows = 1,
unpack=True)

ID, max_offset, ff_slope, max_slope, ms_x, ms_y, ms_z, fault_x, fault_y, fault_z =
loadtxt(slope_file, delimiter = ',', skiprows = 1, unpack=True)

#create a place to store x_start, y_start, x_end, and y_end
x_start = []
y_start = []
x_end = []
```

```
y_end = []

#calculate the slope of perpendicular line to point
for i in range(0, len(max_offset)-1):
        if i == 0:
                m = -(fault_x[i+1] - fault_x[i]) / (fault_y[i+1] - fault_y[i])
        elif i == (len(fault_x)-1):
                m = -(fault_x[i] - fault_x[i-1]) / (fault_y[i] - fault_y[i-1])
        else:
                m = -(fault_x[i+1] - fault_x[i-1]) / (fault_y[i+1] - fault_y[i-1])
        if max_offset[i] > 80:
                offset = 0
        elif max_offset[i] < 0:
                offset = 0
        else:
                offset = max_offset[i]
        x_s = fault_x[i]
        y_s = fault_y[i]
        x_e = fault_x[i] + cos(arctan(m)) * offset
        y_e = fault_y[i] + sin(arctan(m)) * offset
        x_start.append(x_s)
        y_start.append(y_s)
        x_end.append(x_e)
        y_end.append(y_e)

#Create path and filename to store stem data
f = 'path/filename.txt'
target = open(f, 'w')

target.write('ID,max_offset,x_start,y_start,x_end,y_end')
target.write('\n')

for i in range(0, len(max_offset)-1):
        a = str(ID[i])
        b = str(max_offset[i])
        c = str(x_start[i])
        d = str(y_start[i])
        e = str(x_end[i])
        f = str(y_end[i])
        target.write(a)
        target.write(',')
        target.write(b)
        target.write(',')
        target.write(c)
        target.write(',')
        target.write(d)
```

```
        target.write(',')
        target.write(e)
        target.write(',')
        target.write(f)
        target.write('\n')

target.close()
```

REFERENCES

Andrews, D. J., Bucknam, R.C., 1987, Fitting degradation of shoreline scarps by a nonlinear diffusion model: Geophysical Research, Vol. 92, pp.12857–12867.

Arrowsmith, J.R., Glenn, N., Crosby, C.J., Cowgill, E., 2008, Current capabilities and community needs for software tools and educational resources for use with LiDAR high resolution topography data: Electronic document available at http://activetectonics.asu.edu/

Biasi, G.P., Weldon, R.J., 2006, Estimating surface rupture length and magnitude of paleoearthquakes from point measurements of rupture displacement: Bulletin Seimological Society America, Vol. 96, No. 5, pp. 1612-1623.

Biasi, G.P., Weldon, R.J., 2009, San Andreas fault rupture scenarios from multiple paleoseismic records: Stringing pearls: Bulletin Seimological Society America, Vol. 99, No. 2A, pp. 471-498.

Bull, W. B., 1991, Geomorphic responses to climatic change: Oxford University Press, New York, NY, 326 p.

Cavalli, M., Marchi, L., 2008, Characterisation of the surface morphology of an alpine alluvial fan using airborne LiDAR: Natural Hazards Earth System Sciences, Vol. 8, pp. 323-333.

Chang, W., Smith, R.B., 2002, Integrated seismic-hazard analysis of the Wasatch front, Utah: Bulletin Seismological Society America, Vol. 92, No. 5, pp. 1904-1922.

Cowie, P.A., Scholz, C.H., 1992, Growth of faults by accumulation of seismic slip: Journal Geophysical Research, Vol. 97, No. B7, pp. 11,085-11,095.

Crider, J.G., Pollard, D.D., 1998, Fault linkage: Three-dimensional mechanical interaction between echelon normal faults: Geophysical Research. Vol. 103, No. B10, pp. 24,373-24,391.

Crosby, C.J., 2012, Lidar and Google Earth: Simplifying access to high-resolution topography data: Geological Society America Special Papers, Vol. 492, pp. 37-47.

DuRoss, C.B., 2004, Spatial and temporal trends of surface rupturing on the Nephi

segment of the Wasatch fault, Utah: Implications for fault segmentation and the recurrence of paleoearthquakes: Unpublished M.S. Thesis, Department of Geology and Geophysics, University of Utah, Salt Lake City, UT, 120 p.

DuRoss, C.B., 2008, Holocene vertical displacement on the central segments of the Wasatch fault zone, Utah: Bulletin Seismological Society America, Vol. 98, No. 6, pp. 2918-2933.

DuRoss, C.B., Bruhn, R.L., 2005, Active tectonics of the Nephi segment, Wasatch fault, Utah: Basin and Range province seismic hazards summit II: Utah Geological Survey Miscellaneous Publications 05-2, 25 p., CD-ROM.

DuRoss, C.B., McDonald, G.N., Lund, W.R., 2008, Paleoseismic investigation of the northern strand of the Nephi segment of the Wasatch fault zone at Santaquin, Utah: Paeleoseismology Utah, Vol. 17, 33 p.

Frankel, K.L., Dolan, J.F., 2007, Characterizing arid region alluvial fan surface roughness with airborne laser swath mapping digital topographic data: Geophysical Research Letters, Vol. 112, F02025.

Frankel, K.L., Dolan, J.F., Finkel, R.C., Owen, L.A., Hoeft, J.S., 2007, Spatial variations in slip rate along the Death Valley-Fish Lake Valley fault system determined from LiDAR topographic data and cosmogenic ^{10}Be geochronology: Geophysical Research Letters, Vol. 34, No. 18, L18303

Ganas, A., Spyros P., Vassilios, K., 2005, DEM-based morphometry of range-front escarpments in Attica, central Greece, and its relation to fault slip rates: Geomorphology, Vol. 65, pp. 301-319.

Glenn, N.F., Streutker, D.R., Chadwick, D.J., Thackray, G.D., Dorsch, S.J., 2006, Analysis of LiDAR-derived topographic information for characterizing and differentiating landslide morphology and activity: Geomorphology, Vol. 73, No. 1-2, pp. 131-148.

Grohmann, C.H., Smith, M.J., Riccomini, C., 2011, Multiscale analysis of topographic surface roughness in the Midland Valley, Scotland: Transactions Geoscience Remote Sensing, Vol. 49, No. 4, pp. 1200-1213.

Gudmundsson, A., 2003, Effects of Young's modulus on fault displacement: Geoscience, Vol. 336, No. 1, pp. 85-92.

Hanson, K.L., Swan, F.H., and Schwartz, D.P., 1981, Study of earthquake recurrence intervals on the Wasatch fault, Utah: San Francisco, California, Woodward-Clyde Consultants, sixth annual technical report prepared for U.S. Geological Survey under contract no. 14-08-0001-19115, 22 p.

Harding, D.J., Berghoff, G.S., 2000, Fault scarp detection beneath dense vegetation cover: Airborne LiDAR mapping of the Seattle fault zone, Bainbridge Island, Washington State. In Proceedings of the American Society of Photogrammetry and Remote Sensing Annual Conference, Washington, D.C., May, 2000.

Harding, D.J., Blair, J.B., Garvin, J.B., Lawrence, W.T., 1994, Laser altimetry waveform measurement of vegetation canopy structure: Proceedings International Remote Sensing Symposium 1994, Pasadena (CA), California Institute of Technology. pp. 1251-1253.

Harding, D.J., Lefsky, M.A., Parker, G.G., Blair, J.B., 2001, Lidar altimeter measurements of canopy structure: Methods and validation for closed-canopy, broadleaf forests: Remote Sensing Environment, Vol. 76, pp. 283–297.

Harty, K.M., Mulvey, W.E., and Machette, M.N., 1997, Surficial geologic map of the Nephi segment of the Wasatch fault zone, eastern Juab County, Utah: Utah Geological Survey Map 170, 14 p.

Haugerud, R.A., Harding, D.J., Johnson, S.Y., Harless, J.L., Weaver, C.S., 2003, High-resolution Lidar topography of the Puget Lowland – A bonanza for Earth Science, Washington: GSA Today, Vol. 13, pp. 4-10.

Hooper, D.M., Bursik, M.I., Webb, F.H., 2003, Application of high-resolution interferometric DEMs to geomorphic studies of fault scarps, Fish Lake Valley, Nevada–California, USA: Remote Sensing Environment, Vol. 84, No. 2, pp. 255–267.

Hylland, M.D., and Machette, M.N., 2008, Surficial geologic map of the Levan and Fayette segments of the Wasatch fault zone, Juab and Sanpete Counties, Utah: Utah Geological Survey Map 229, 37 p.

Jackson, M., 1991, Paleoseismology of Utah, Volume 3 – Number and timing of Holocene paleoseismic events on the Nephi and Levan segments, Wasatch fault zone, Utah: Utah Geological Survey Special Study 78, 23 p.

Klingebiel, A. A., Horvath, E.H., Reybold, W.U., Moore, D.G., Fosnight, E.A., Loveland, T.R., 1988, A guide for the use of digital elevation model data for making soil surveys: U.S. Geological Survey Open-File Report 88-102, 18 p.

Lin, Z., Kaneda, H., Mukoyama, S., Asada, N., Chiba, T., 2013, Detection of subtle tectonic-geomorphic features in densely forested mountains by very high-resolution airborne LiDAR survey: Geomorphology, Vol. 182, pp. 104-115.

Lund, W.R., 2005, Consensus preferred recurrence-interval and vertical slip-rate estimates – review of Utah paleoseismic- trenching data by the Utah Quaternary Fault Parameters Working Group: Utah Geological Survey Bulletin 130, 109 p.,

compact disk.

Machette, M.N., 1992, Surficial geologic map of the Wasatch fault zone, eastern part of Utah Valley, Utah County and parts of Salt Lake and Juab Counties, Utah: U.S. Geological Survey Miscellaneous Investigations Series Map I- 2095, 30 p.

Machette, M.N., Crone, A.J., Personius, S.F., Mahan, S.A., Dart, R.L., Lidke, D.J., Olig, S.S, 2007, Paleoseismology of the Nephi Segment of the Wasatch fault zone, Juab County, Utah - Preliminary results from two large exploratory trenches at Willow Creek: USGS Scientific Investigations Map: 2966

Mattson, A., and Bruhn, R.L., 2001, Fault slip rates and initiation age based on diffusion equation modeling – Wasatch fault zone and eastern Great Basin: Journal Geophysical Research, Vol. 106, No. B7, pp. 13,739–13,750.

McCalpin, J.P., 2009, Paleoseismology: Academic Press, Burlington, MA, 848 p.

Olig, S. S., 1994, Seismic hazard evaluation—Kennecott tailings impoundment modernization project, Magna, Utah, unpublished report, Woodward-Clyde Consultants, C1–C6.

Pavlis, T.L., Bruhn, R.L., 2011, Application of LIDAR to resolving bedrock structure in areas of poor exposure: An example from the STEEP study area, southern Alaska: GSA Bulletin, Vol. 123, No. 1-2, pp. 206-217.

Pezzopane, S. K., and Dawson T. E., 1996, Fault displacement hazard: a summary of issues and information, U.S. Geological Survey Yucca Mountain Report to the U.S. Department of Energy: Seismotectonic Framework and Characterization of Faulting at Yucca Mountain, Nevada, Chapter 9, 160 pp.

Robinson, J.E., Bacon, C.R., Wayne, C., 2012, Under trees and water at Crater Lake National Park, Oregon: U.S. Geological Survey Scientific Investigations Map 3223.

Sagy, A., Brodsky, E.E., Axen, G.J., 2007, Evolution of fault-surface roughness with slip: Geology, Vol. 35, No. 3, pp. 283-286.

Sanders, C.O., Slemmons, D.B., 1996, Geomorphic evidence for Holocene earthquakes in the Olinghouse fault zone, Western Nevada: Bulletin Seismological Society America, Vol. 86, No. 6, pp. 1784 – 1792.

UNAVCO, 2008, UNAVCO LiDAR Campaign, Yellowstone, Wasatch and Alaska fault systems, Processing Report: 22 p.

U.S. Geological Survey, 1993, Digital elevation models: U.S. Geological Survey Data User's Guide 5, 53 p.

U.S. Geological Survey, Utah Geological Survey, Idaho Geological Survey, 2006, Quaternary fault and fold database for the United States: Electronic document, available at http//earthquakes.usgs.gov/regional/qfaults/

Wallace, R.E., 1977, Profiles and ages of young fault scarps, north-central Nevada: Geological Society America Bulletin, Vol. 88, pp. 1267-1281.

Walsh, J.J., Watterson, J., 1988, Analysis of the relationships between displacements and dimensions of faults: Journal Structural Geology, Vol. 10, pp. 239-247.

Watterson, J., 1986, Fault dimensions, displacements and growth: Pure Applied Geophysics, Vol. 124, pp. 365-373.

Webster, T.L., Murphy, J.B., Gosse, J.C., 2006, Mapping subtle structures with light detection and ranging (LIDAR): flow units and phreatomagmatic rootless cones in the North Mountain Basalt, Nova Scotia: Canadian Journal Earth Sciences, Vol. 43, pp. 157-176.

Wells, D.L., Coppersmith, K.J., 1994, New empirical relationships among magnitude, rupture length, rupture width, rupture area, and surface displacement: Bulletin Seismological Society America, Vol. 84, No. 4, pp. 974-1002.

Wells, S. G., McFadden, L.D., Dohrenwend, J.C., 1987, Influence of late Quaternary climatic changes on a desert piedmont, eastern Mojave desert, California: Quaternary Research, Vol. 27, pp. 130–146.

Zhang, K., Whitman, D., 2005, Comparison of three algorithms for filtering airborne lidar data: Photogrammetric Engineering Remote Sensing, Vol. 71, pp. 313-324.

Zielke, O., 2009, LaDiCaoz: A MATLAB graphical user interface to calculate the lateral displacement of offset geomorphic features: Electronic document, available at https://cloud.sdsc.edu/v1/AUTH_opentopography/www/shortcourses/09SCEC_co urse/LaDiCaoz_Tutorial2.pdf